

Ocean Surface Roughness Spectrum in High Wind Condition for Microwave Backscatter and Emission Computations*

PAUL A. HWANG

Remote Sensing Division, Naval Research Laboratory, Washington, D.C.

DEREK M. BURRAGE, DAVID W. WANG, AND JOEL C. WESSON

Oceanography Division, Naval Research Laboratory, Stennis Space Center, Mississippi

(Manuscript received 15 November 2012, in final form 15 April 2013)

ABSTRACT

Ocean surface roughness plays an important role in air–sea interaction and ocean remote sensing. Its primary contribution is from surface waves much shorter than the energetic wave components near the peak of the wave energy spectrum. Field measurements of short-scale waves are scarce. In contrast, microwave remote sensing has produced a large volume of data useful for short-wave investigation. Particularly, Bragg resonance is the primary mechanism of radar backscatter from the ocean surface and the radar serves as a spectrometer of short surface waves. The roughness spectra inverted from radar backscatter measurements expand the short-wave database to high wind conditions in which in situ sensors do not function well. Using scatterometer geophysical model functions for L-, C-, and Ku-band microwave frequencies, the inverted roughness spectra, covering Bragg resonance wavelengths from 0.012 to 0.20 m, show a convergent trend in high winds. This convergent trend is incorporated in the surface roughness spectrum model to improve the applicable wind speed range for microwave scattering and emission computations.

1. Introduction

The study of ocean surface roughness is of interest in a wide range of research areas including wind wave generation, air–sea interaction, gas exchange, and ocean remote sensing. On the ocean surface, surface water waves are the roughness elements. The length scales of the ocean surface roughness, in terms of the mean square slopes (Cox and Munk 1954; Jackson et al. 1992; Walsh et al. 1998; Vandemark et al. 2004; Hwang 2005, 2008; Hauser et al. 2008) or with respect to the Bragg resonance wave components relevant to microwave remote sensing (e.g., Wright 1966; Valenzuela 1978), are of subcentimeter to meter wavelengths. These are much shorter than the energetic wave components near the

peak of the wave energy spectrum. To distinguish from the energy-containing portion of the “wave spectrum” we use the term “roughness spectrum” to emphasize the slope-contributing short-scale waves. The mechanisms governing short-wave evolution are rather complex. As will be further discussed in section 2, comprehensive theoretical or numerical models governing the dynamics of the ocean surface roughness sufficient for operational applications remain to be constructed.

Obtaining measurements in the ocean environment for developing an empirical description of the surface roughness properties is also a challenging task. Cox and Munk (1954) present an extensive dataset on the statistical properties of the spectrum-integrated surface roughness (the upwind and crosswind mean square slopes) through the analysis of airborne measurements of sun glitter patterns. More recent optical observations of mean square slopes (e.g., Ebuchi and Kizu 2002; Bréon and Henriot 2006; Ross and Dion 2007) generally confirm the results of Cox and Munk (1954); see also a review by Munk (2009) on the subject. Similar techniques are used for measuring the low-pass-filtered mean square slopes using radars of different frequencies

*U.S. Naval Research Laboratory Contribution Number JA/7260-12-0254.

Corresponding author address: Dr. Paul A. Hwang, Remote Sensing Division, Naval Research Laboratory, 4555 Overlook Avenue SW, Washington, DC 20375.
E-mail: paul.hwang@nrl.navy.mil

operated in the near-nadir-looking configuration (e.g., Jones and Schroeder 1978; Wentz 1977; Jackson et al. 1992; Walsh et al. 1998; Vandemark et al. 2004; Hauser et al. 2008).

Cox (1958) reports laboratory measurements of high-frequency waves using an optical apparatus that yields the time series of the surface wave slope component in the wind direction. Measurement techniques have advanced significantly and many studies of one-dimensional (1D) and 2D wavenumber spectra of wind-generated waves in laboratory facilities have been reported (e.g., Jähne and Riemer 1990; Hwang et al. 1993; Zhang 1995, 2003, 2005).

In situ measurements of temporal or spatial series and spectrum of short waves in the ocean are much more difficult to acquire. Several decades after Cox and Munk's sun glitter data (1954) and Cox's time series measurements in the laboratory (1958), a small quantity of short-wave frequency spectra were obtained by laser slope sensors mounted on wave-following platforms deployed in the ocean (e.g., Hughes and Grant 1978; Tang and Shemdin 1983; Caponi et al. 1988; Shemdin and Hwang 1988). Interpretation of the short-wave frequency spectrum is difficult because of the large Doppler frequency shift caused by the random ocean surface currents advecting the short waves (e.g., Hwang 2006). Shemdin et al. (1988) and Banner et al. (1989) report wavenumber spectrum measurements using stereo photography. The range of resolved wavelengths is between 0.03 and 2.5 m for the former (3 cases, wind speeds less than 5 m s^{-1}) and between 0.2 and 1.6 m for the latter (4 cases, wind speeds between 5.5 and 13.3 m s^{-1}). Scanning laser slope sensing systems and optical imaging devices on fixed, towed, or free-drifting platforms have been developed to measure the wavenumber spectrum directly (Bock and Hara 1995; Klinke and Jähne 1995; Hwang et al. 1996; Hara et al. 1998). The scanning laser slope sensing systems are designed to resolve very short waves, typically between about 0.004 and 0.2 m in wavelength. The ocean surface mean square slope is contributed mainly by waves between 0.001 and 10 m long, whereas the Bragg resonance wavelengths most relevant to ocean remote sensing using microwave frequencies are between about 0.01 and 0.3 m. The tilting components important to the microwave computation are several times longer than the Bragg length scale. Therefore, broadband coverage of several orders of magnitude, from millimeter to decameter wavelengths, is critical to understanding the ocean surface roughness. More recently, Zappa et al. (2008, 2012) present preliminary results of wavenumber spectrum measurements using an optical polarimetric imaging technique that show the promise of resolving a broad range of wavelength scales.

To expand the range of wavenumber coverage, Hwang and Wang (2004a) adopt a different approach: they obtain time series and frequency spectra using a wave gauge array system on a free-drifting platform deployed in the ocean environment. The free-drifting operation is designed to alleviate the problem of Doppler frequency shift related to frequency–wavenumber conversion of the short-scale wave spectrum (Hwang and Wang 2004a; Wang and Hwang 2004). A composite short-wave dataset of 397 spectra was assembled from several deployments of the system in the ocean. The wind speed in the dataset ranges from 2.6 to 14.2 m s^{-1} , and the resolved wavelength range is from 0.02 to 6 m, or a wavenumber from about 1 to 300 rad m^{-1} . These data, sorted into the wind sea and mixed sea groups, form the foundation of a parameterization function of the ocean surface roughness spectrum: $B(k) = A(k)(u_*c^{-1})^{a(k)}$, where B is the 1D dimensionless wavenumber spectrum, u_* is the wind friction velocity, c is the wave phase speed, and k is the wavenumber (Hwang 2005). Extending the spectrum coverage beyond the data range toward both longer and shorter scales relies on assuming asymptotic functions for $A(k)$ and $a(k)$ toward the two ends of the wavenumber range (Hwang 2008, 2011). Section 2 presents a brief description of the ocean surface roughness spectrum parameterization, with additional discussions given in section 5a and the appendix.

Parallel to in situ measurements, microwave remote sensing makes considerable contributions to the understanding of short-scale waves, in addition to the mean square slope measurements described earlier. Bragg resonance was identified as a dominant mechanism of radar backscatter from the ocean surface more than a half century ago (Crombie 1955), and microwave radars have been used to measure short waves and to investigate their dynamics (e.g., Wright 1966, 1968, 1978; Keller and Wright 1975; Plant 1977; Plant and Wright 1977, 1979, 1980). Of special interest to the present discussion is the robust Bragg resonance mechanism governing the vertical polarization radar backscatter. The microwave radar serves as a surface wave spectrometer for extracting the short-scale wave spectrum from the large quantity of backscatter measurements (e.g., Wright 1968; Chaudhry and Moore 1984). Section 3 outlines an approach to obtain the parameterization factors of the surface roughness spectrum using the geophysical model functions (GMFs), which empirically relate the wind velocity and microwave normalized radar cross section (NRCS), established with airborne and spaceborne scatterometer measurements at Ku, C, and L bands. The combination of the three microwave frequency bands provides a good coverage of the roughness wavelength components (about a factor of 16, with k ranging from 31 to 508 rad m^{-1} or wavelengths

between 0.20 and 0.012 m) and extends the wind speed coverage into stormy conditions. The analysis shows that the roughness spectrum parameterization factors derived from in situ and remote sensing measurements are in close agreement for low and moderate wind speeds (less than about 15 m s^{-1}). The roughness spectra inverted from the three GMFs converge to $B(u_*c^{-1}; k) \sim (u_*c^{-1})^{0.75}$ for higher wind speeds (u_*c^{-1} greater than about 3; because the minimum phase speed of surface water waves is 0.23 m s^{-1} , the minimum wind speed for $u_*c^{-1} > 3$ is about 16 m s^{-1}). Thus the power-law roughness spectrum parameterization function can be extended to high winds by taking into account the similarity property that the wind speed exponent becomes independent on wavenumber toward high winds. The detail is described in section 3.

At the present time, a comprehensive dataset of short-scale wave spectra obtained in field conditions using conventional wave measurement techniques does not exist. One way to assess the validity of the parameterized roughness spectrum model is by comparing the active and passive microwave simulations using the roughness spectrum to the field measurements. For the active radar, the Ku-, C-, and L-band GMFs serve as a proxy of field data. The upper-bound applicable wind speeds of the GMFs are about $50\text{--}70 \text{ m s}^{-1}$ for C- and Ku-band GMFs and somewhat less for the L band (about $20\text{--}30 \text{ m s}^{-1}$). For the passive radiometer, the wind effects on the brightness temperature simulated with the parameterized roughness spectrum can be compared with global WindSat measurements reported by Meissner and Wentz (2009); the upper-bound wind speed in the dataset is about 42 m s^{-1} . Both active and passive microwave simulations using the proposed roughness spectrum model are in good agreement with the satellite measurements (section 4). Several issues on the parameterization approach of the roughness spectrum model are discussed in section 5, and a summary is given in section 6.

2. Ocean surface roughness spectrum parameterization

a. Background

As mentioned in section 1, the length scales of the ocean surface roughness most relevant to microwave remote sensing are of subcentimeter to meter wavelengths. Most of the research on surface wave dynamics and kinematics concerns the energetic portion of the wave spectrum with peak wavelengths several tens to a few hundred meters. The results from the extensive research efforts of the energetic surface waves may not

be readily applicable to the short-scale waves. For example, for the energetic long waves, the three major source functions of the wave energy or wave action conservation equation are wind input, wave breaking dissipation, and four-wave nonlinear resonance interaction. For short waves of centimeter and subcentimeter length scales, nonlinear resonance interaction occurs at the three-wave level (e.g., McGoldrick 1965, 1970; Simmons 1967; Dias and Kharif 1999) and wave breaking is in fact more of a generation term than a dissipation term (Hwang 2007, 2011). The laboratory observation of the train of capillary waves near the crests of dominant gravity waves (Cox 1958) led to the development of a theory of nonlinear energy transfer from steep short gravity waves to capillary waves (Longuet-Higgins 1963, 1992), and it represents an important generation source function unique to the capillary waves. Surface roughness representation of intermittent breaking impulses and plumes (Longuet-Higgins and Turner 1974) and the subsequent impulse-/plume-produced short-wave generation remain difficult to quantify and model. Observations showing a nonuniform distribution (almost sawtoothlike) of the surface wind stress along the wind wave profile (e.g., Okuda et al. 1977) further complicate the representation of the wind generation source function for short waves. Spectral investigations of short surface waves up to this date are mainly designed to investigate individual mechanisms, especially the nonlinear interaction term, and usually incorporate only very crude representations of the various source functions or in some cases ignore many sources functions entirely (e.g., Valenzuela and Laing 1972; Janssen 1987; van Gastel 1987; Zhang 1995; Stiassnie 1996; Kudryavtsev et al. 1999; Dulov and Kosnik 2009). It is fair to say that a comprehensive theoretical or numerical model suitable for operational computation of the roughness spectrum is not yet available.

With respect to parameterizing the surface roughness spectrum for microwave computations, the equilibrium or saturation spectrum models of short waves (Phillips 1958, 1985) are frequently used to describe the Bragg resonance components (e.g., Wright 1966, 1968). Many full spectrum surface wave models have been proposed over the years (e.g., Pierson and Stacy 1973; Bjerkaas and Riedel 1979; Fung and Lee 1982; Chaudhry and Moore 1984; Durden and Vesecky 1985; Donelan and Pierson 1987; Shemdin and Hwang 1988; Apel 1994; Elfouhaily et al. 1997; Romeiser et al. 1997; Kudryavtsev et al. 1999; Plant 2002; Hwang 2005, 2008, 2011). Some of these models are anchored on the dominant wave portion of the spectrum, of which plenty of field data exist. The short-wave portion is treated as a high-frequency extension of the dominant wave spectrum with parameterizations

using mostly laboratory measurements of short waves or limited amount of field data. A few spectrum models make extensive use of radar backscatter observations for the short-wave portion of the spectrum. Several comparisons of the various spectrum models are summarized at the end of this section.

b. Our strategy of modeling the roughness spectrum

Considering that the contribution of the mean square slope from short-scale waves is much larger than that from the long waves, the roughness spectrum model proposed by Hwang (2005) emphasizes the parameterization of the wave components in centimeter to meter wavelengths with data collected in the ocean covering k between 1 and 300 rad m^{-1} (Hwang and Wang 2004a). The parameterization design is derived from the source function balance analysis of short surface gravity waves (Phillips 1984). Particularly, Phillips concludes that the knowledge of the functional dependence of the dimensionless wavenumber spectrum $B(k)$ on the dimensionless wind speed u_*c^{-1} is of great relevance to understanding the properties of short-scale surface waves. The factor u_*c^{-1} characterizes the wind wave generation process (e.g., Miles 1957; Plant 1982; Phillips 1985) and can be interpreted as a wind forcing parameter. The analysis of the short-wave spectra measured in the ocean covering wavenumbers between 1 and 300 rad m^{-1} yields an empirical power-law function (Hwang and Wang 2004a):

$$B\left(\frac{u_*}{c}; k\right) = A(k) \left(\frac{u_*}{c}\right)^{a(k)}. \tag{1}$$

The 1D dimensionless spectrum is related to the wave elevation spectrum by $B(k) = k^3 F(k)$, where $F(k) = \int_{-\pi}^{\pi} S(k, \phi) k d\phi$, $F(k)$ and $S(k, \phi)$ are, respectively, the 1D and 2D elevation spectrum [i.e., $\int_0^{\infty} F(k) dk$ and $\int_0^{\infty} \int_{-\pi}^{\pi} S(k, \phi) k dk d\phi$ yield the variance of the surface elevation $\langle \eta^2 \rangle$], and ϕ is the wave propagation angle with respect to the wind direction.

Although the original analysis of Phillips (1984) is for short gravity waves, based on analyzing the microwave backscatter data (section 3) the empirical parameterization function (1) is applicable to capillary waves also. As commented earlier, the factor u_*c^{-1} represents wind forcing, and it characterizes the wind generation source function (e.g., Miles 1957; Plant 1982; Phillips 1985). Another important source mechanism of short waves is the generation of parasitic capillary waves by the localized surface tension forces near the wave crests induced by steep short gravity waves (Longuet-Higgins 1963, 1992; Ebuchi et al. 1987). The steepness of short wind waves is also closely associated with the factor u_*c^{-1} . It

remains unclear how to rank the nonlinear wave–wave interaction mechanism in capillary wave evolution, although there have been many papers on the subject (section 2a); for short gravity waves, the nonlinear interaction term is relatively small compared to wind generation and breaking dissipation terms (Phillips 1984). In any case, the factor u_*c^{-1} will stand out for both short gravity and capillary waves since the balance of source functions involves at least two major generation mechanisms characterized by u_*c^{-1} .

Because c and k are related by the surface wave dispersion relationship $c^2 = gk^{-1} + \tau k$, where g is the gravitational acceleration and τ is the surface tension divided by water density, $B(u_*c^{-1}; k)$ is a useful parameterization function of the ocean surface roughness spectrum. In practice, a matrix of $B(u_*c^{-1}; k)$ is computed for a range of u_* and k with (1). Expressed as $B(u_*, k)$, the result describes $B(u_*)$ for a given k or $B(k)$ for a given u_* , which is the dimensionless wave spectrum for a given wind friction velocity. The surface roughness spectrum derived from this approach is referred to as the H spectrum in this paper. Hwang (2005) presents $A(k)$ and $a(k)$ as lookup tables to facilitate the computation of $B(u_*c^{-1}; k)$. Hwang (2008, 2011) further simplifies the computational procedure by developing analytical functions for $A(k)$ and $a(k)$ with k coverage extending virtually from 0 to ∞ . The complete parameterization functions of $A(k)$ and $a(k)$ are given in section 2 of Hwang (2011) and summarized in the appendix; this formulation is referred to as the H11 algorithm.

In many applications, it is preferred to use the reference wind speed U_{10} as input, for which a formula for the drag coefficient $C_{10} = u_*^2 U_{10}^{-2}$ is needed. Recent drag coefficient data suggest that a saturation trend may occur near $U_{10} = 35 \text{ m s}^{-1}$, with a subsequent decrease potentially occurring in higher wind speeds. By least squares fitting field data obtained in three open ocean experiments (Felizardo and Melville 1995; Powell et al. 2003; Jarosz et al. 2007), Hwang (2011, 2012) employs the following empirical equation that captures the saturation and decaying behavior of the drag coefficient in high winds (Fig. 1):

$$C_{10} = 10^{-5}(-0.16U_{10}^2 + 9.67U_{10} + 80.58). \tag{2}$$

The computed wind friction velocity u_* increases monotonically with U_{10} up to 50 m s^{-1} and then decreases for $U_{10} > 50 \text{ m s}^{-1}$ (Fig. 1b). It is recognized that there is still considerable uncertainty in the ocean surface drag coefficient in high winds. For example, Vickery et al. (2009) and Holthuijsen et al. (2012) show that the leveling off or decreasing of C_{10} in high winds may be influenced by many factors such as the radius of the storm, the

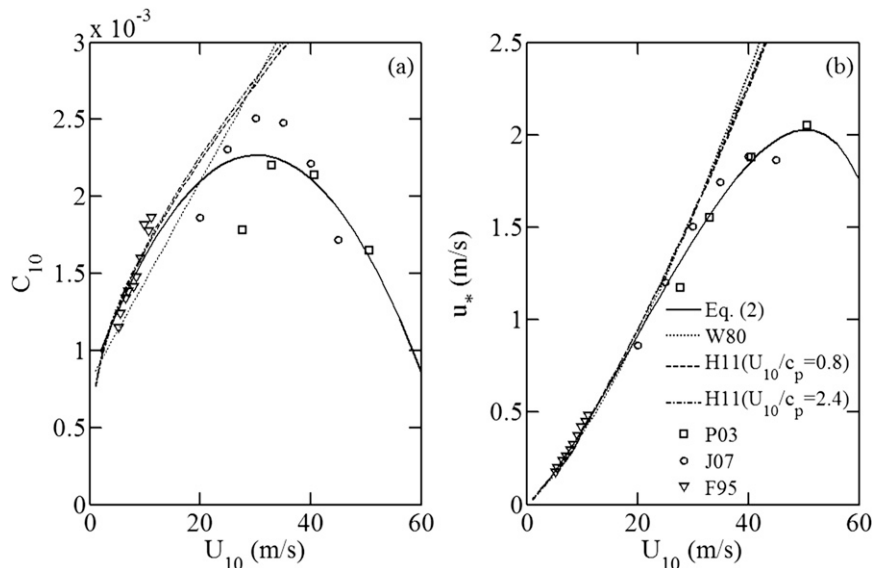


FIG. 1. (a) Examples of the functions describing the wind speed and sea state dependence of the ocean surface drag coefficient from Wu (1980; W80) and Hwang et al. (2011b; H11) and comparison with three open ocean datasets used for the empirical fitting function (2) from Felizardo and Melville (1995; F95), Powell et al. (2003; P03), and Jarosz et al. (2007; J07). (b) As in (a), but for friction velocity as a function of wind speed.

relative location of the region of measurements with respect to the storm center, and the direction of storm motion. Results extrapolated beyond about 50 m s^{-1} wind speed need to be treated with caution.

Presently, there are many formulas for C_{10} [e.g., see reviews by Wu (1980), Donelan (1990), and Geernaert (1990)]. Hwang et al. (2011b) show that for both wind sea and mixed sea conditions, a similarity relationship exists between $C_{\lambda/2}$ and ω_{**} or $\omega_{\#}$: $C_{\lambda/2}$ is the ocean surface drag coefficient referenced to the neutral wind speed at an elevation equal to one-half of the wavelength of the frequency spectrum peak component, and $\omega_{**} = \omega_p u_* / g$ and $\omega_{\#} = \omega_p U_{10} / g$ represent the dimensionless wave spectrum peak frequency but with different wind speed scaling. The drag coefficient C_{10} can be derived with U_{10} and ω_p or k_p input using the $C_{\lambda/2}$ similarity relationship. Figure 1a shows the C_{10} curves of Wu (1980) and Hwang et al. (2011b) for $\omega_{\#} = 0.8$ and 2.4 in mixed seas. The computed u_* is clearly sensitive to the choice of C_{10} formulas, especially in high winds (Fig. 1b). Section 5b presents a more extensive discussion on the drag coefficient and its impact on microwave computations.

c. A brief summary of roughness spectrum comparisons

As outlined in the beginning of this section, there are many full spectrum models proposed in the literature. To our knowledge, no comprehensive comparison studies of

all the spectrum models have been reported because of the large number of models in existence. Many smaller-scale comparisons have been documented. For example, Shemdin and Hwang (1988) compare their empirical model, based on field measurements of frequency spectra using a laser slope sensor carried on a wave follower, with the spectrum models of Pierson and Stacy (1973) and Donelan and Pierson (1987). Elfouhaily et al. (1997) compare their spectrum model with those of Donelan and Pierson (1987) and Apel (1994). Romeiser et al. (1997) compare their spectrum model with those of Bjerkaas and Riedel (1979) and Apel (1994). Plant (2002) compares the Elfouhaily et al. (1997) spectrum and a variation of the Donelan and Pierson (1987) spectrum with modifications by Banner (1990) and Plant (2002), who named the two spectrum models E and D, respectively. Most spectrum models produce reasonable agreement in the integrated mean square slopes in comparison with those reported by Cox and Munk (1954), but discrepancies in the spectral distribution in the wavenumber space among various spectrum models are obvious.

Hwang and Plant (2010) describe a comparison study of radar backscattering NRCS computation using three roughness spectrum models (D, E, and H). Hwang et al. (2011a) report radiometer brightness temperature simulations using the D, E, H, and K spectrums; K is for Kudryavtsev et al. (1999). They also include the DV spectrum (Durden and Vesecky 1985) in the comparison

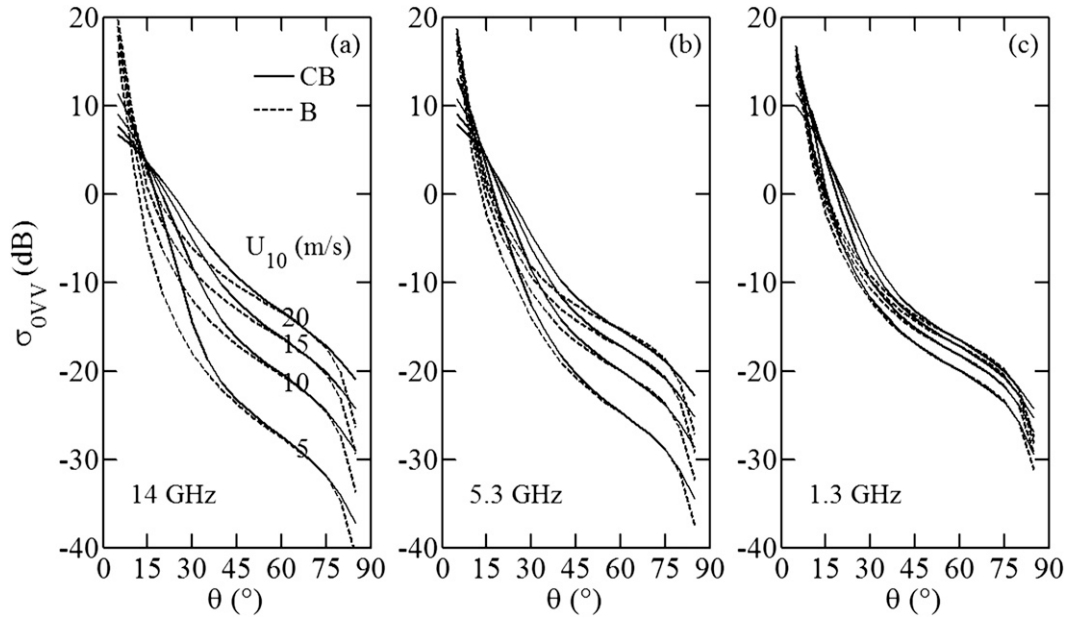


FIG. 2. Solutions of B and CB resonance radar backscatter from the ocean surface, (a) Ku band (14 GHz), (b) C band (5.3 GHz), and (c) L band (1.3 GHz).

of the wind speed dependence of the spectral densities of representative L- and K-band Bragg resonance components (30 and 405 rad m^{-1} , respectively). In these two studies, the mean square slopes integrated over four different bands are compared with the available optical measurements and radar data collected with Ka-, Ku-, and C-band microwave frequencies. The H spectrum performs very well in these comparison studies. Further verification of the H spectrum extending to the high wind condition is given in section 4.

3. Radar as a surface roughness spectrometer

a. Radar backscatter and surface roughness

The Bragg resonance was identified as an important mechanism of radar backscatter from the water surface more than a half century ago (Crombie 1955). The solution of the Bragg resonance backscatter is (e.g., Valenzuela 1978; Plant 1990)

$$\sigma_{0pq}(\theta) = 16\pi k_r^4 \cos^4\theta |g_{pq}(\theta)|^2 S(k_B, 0), \quad (3)$$

where σ_0 is the radar backscattering cross section per unit area of the sea surface (i.e., the NRCS), subscripts p and q denote transmitting and receiving polarizations and can be V (vertical) or H (horizontal), k_r is the radar wavenumber, θ is the incidence angle, $k_B = 2k_r \sin\theta$ is the wavenumber of the Bragg resonance surface wave component, and g_{pq} is the scattering coefficient.

In a wave field with multiple spectral wave components, the short waves in Bragg resonance are tilted by long waves, as described by the composite-surface Bragg (also called the two-scale or tilted Bragg) scattering model (e.g., Valenzuela 1978; Plant 1990). The surface tilting produces cross polarization, causes the local incidence angle θ_i to deviate from the nominal incidence angle θ referenced to a horizontal surface, and modifies the Bragg resonance roughness spectral components as a result of the change in the local incidence angle. Accounting for all the surface tilting effects, then

$$\sigma_{0pq}(\theta) = \int_{-\infty}^{\infty} \int_{-\infty}^{\infty} \sigma_{0pq}(\theta_i) p(\tan\psi, \tan\xi) d(\tan\xi) d(\tan\psi), \quad (4)$$

where $p(\tan\psi, \tan\xi)$ is the probability density function (PDF) of the tilting ocean surface slopes, and ψ and ξ are the angles of the tilting surface in and perpendicular to the radar incidence plane. More details on our implementation of the composite-surface Bragg scattering model are given in Hwang et al. (2010).

Figure 2 shows the VV NRCS at 5, 10, 15, and 20 m s^{-1} wind speeds, calculated with the Bragg (B) and composite-surface Bragg scattering (CB) solutions for Ku-, C-, and L-band radar frequencies (14, 5.3, and 1.3 GHz, respectively) using the ocean surface roughness spectrum described in Hwang (2011) and the Gram-Charlier PDF (Cox and Munk 1954) for the tilting surface slopes. Within the range of about 45°–75° incidence

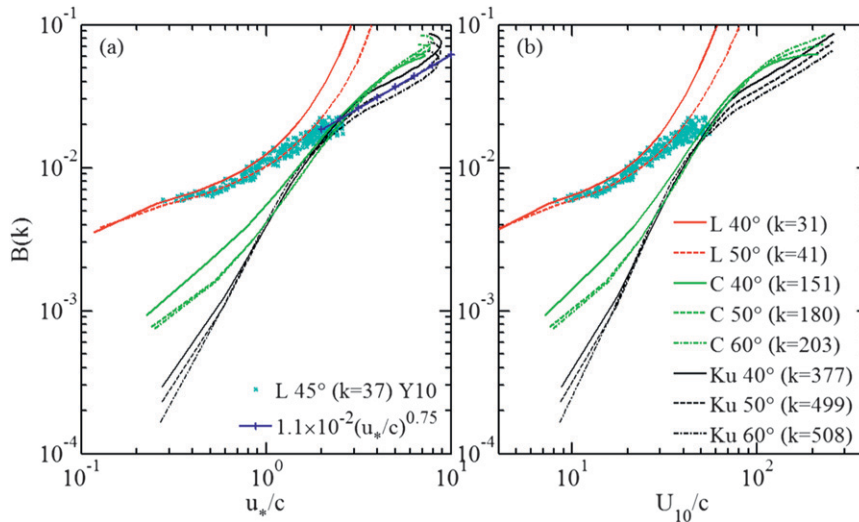


FIG. 3. (a) Ocean surface roughness spectrum $B(u_*c^{-1}; k)$ retrieved from normalized radar cross sections at $\theta = 40^\circ, 50^\circ,$ and 60° and $U_{10} = 2\text{--}60 \text{ m s}^{-1}$ for Ku2001 and CMOD5) and at $\theta = 40^\circ$ and 50° and $U_{10} = 2\text{--}20 \text{ m s}^{-1}$ for the L-band GMF. The result from retrieval using the L-band scatterometer data of Yueh et al. (2010) at 45° incidence angle is also displayed (labeled as Y10). In high winds ($u_*c^{-1} > 3$), $B(u_*c^{-1}; k) \sim (u_*c^{-1})^{0.75}$ is illustrated by the blue ticked line. (b) As in (a), but presented in terms of $B(U_{10}c^{-1}; k)$.

angles (the range may differ slightly depending on wind speed and microwave frequency), the B and CB solutions are very close and the Bragg solution [in (3)] can be used to retrieve the surface roughness spectral information using measurements of the radar cross section. Making use of the Bragg wavenumber equation $k_B = 2k_r \sin\theta$, the VV NRCS in (3) can be rewritten in terms of the 2D dimensionless roughness spectrum $B(k, \phi) = k^4 S(k, \phi)$ as

$$\sigma_{0VV}(\theta, \phi_B) = \frac{\pi}{\tan^4\theta} |g_{VV}(\theta)|^2 B(k_B, \phi_B), \quad (5)$$

which leads to

$$B(k_B) = \frac{\sigma_{0VV}(\theta) \tan^4\theta}{\pi |g_{VV}(\theta)|^2}, \quad (6)$$

where $B(k) = k^4 S(k) = k^3 F(k)$, $S(k) = \int_{-\pi}^{\pi} S(k, \phi) d\phi$, and both $\sigma_{0VV}(\theta)$ and $B(k_B)$ are averaged azimuthally. The directional distribution functions developed in the Donelan–Banner–Plant (D spectrum) model (Donelan et al. 1985; Banner 1990; Plant 2002) are used together with the 1D $B(k)$ described in the last section for the microwave computation; see Hwang and Plant (2010) and Hwang et al. (2010) for more discussion.

b. Roughness spectrum inversion using geophysical model functions

Presently, the GMFs for Ku, C, and L frequency bands are better developed than other frequencies. The

following computations are based on the Ku2001 GMF (Wentz and Smith 1999; D. Smith 2009, personal communication), C-band GMF (CMOD5; Hersbach et al. 2007), and L-band GMF (Isoguchi and Shimada 2009; Yueh et al. 2010). The Ku2001 GMF is given as lookup tables of $\sigma_{0pp}(\theta, U_{10}, \phi)$, with θ from 16° to 66° in 0.5° intervals, U_{10} from 0 to 70 m s^{-1} in 0.2 m s^{-1} intervals, ϕ from 0° to 180° in 2° intervals, and pp for VV and HH polarizations. The CMOD5 and L-band GMFs are given as analytical functions expressing the NRCS as second-order cosine harmonic functions of the radar azimuthal angle (with respect to the wind direction). Figure 3a shows $B(u_*c^{-1}; k)$ retrieved with (5) applied to the three GMFs, the corresponding $B(U_{10}c^{-1}; k)$ is given in Fig. 3b. Interestingly, in contrast to $B(U_{10}c^{-1}; k)$, $B(u_*c^{-1}; k)$ becomes double valued in high winds. This is a consequence of the assumed C_{10} function (2) and will be further discussed in section 5b.

The incidence angles and wind speed range used in the computation of Ku2001 and CMOD5 are $\theta = 40^\circ, 50^\circ,$ and 60° and U_{10} from 2 to 60 m s^{-1} . The corresponding Bragg resonance wavenumbers for the three incidence angles are 377, 499, and 508 rad m^{-1} for the Ku band and 151, 180, and 203 rad m^{-1} for the C band. The L-band database is more limited (Isoguchi and Shimada 2009) and the computation is performed for $\theta = 40^\circ$ and 50° (Bragg wavenumbers 31 and 41 rad m^{-1}) and U_{10} from 2 to 20 m s^{-1} . Although Fig. 2 suggests that the best θ range for spectral inversion using the simple Bragg

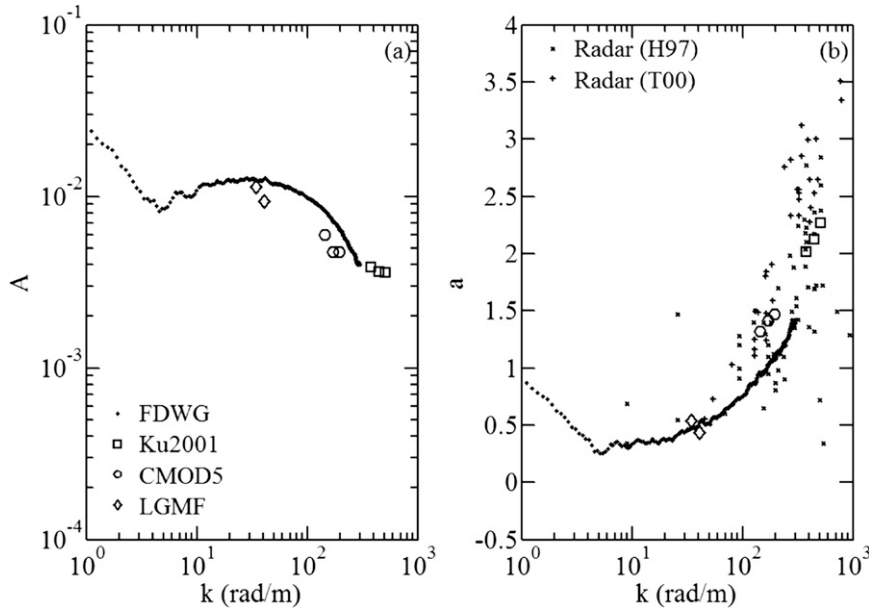


FIG. 4. (a) $A(k)$ and (b) $a(k)$ of the roughness spectrum parameterization function; results displayed are from inversion of NRCS (Fig. 3) and analysis of wave spectra measured by FDWGs in the ocean (Hwang and Wang 2004a). Also shown in (b) is the NRCS wind speed exponents as summarized in Fig. 5 of Hwang (1997) and Fig. 4 of Trokhimovski and Irisov (2000), labeled as H97 and T00, respectively.

resonance solution (3) is from 45° to 75° , the actual calculation takes into consideration the recommended θ application range for each GMF: from 16° to 66° for Ku2001, from 18° to 58° for CMOD5, and from 17° to 43° for L band. Also shown in Fig. 3 are the L-band scatterometer measurements reported by Yueh et al. (2010), covering wind speeds from 4 to 28 m s^{-1} (available for $\theta = 45^\circ$ only). In high winds, the result of the L-band GMF of Isoguchi and Shimada (2009) deviates considerably from Yueh et al. (2010) dataset; the latter is considered to be more accurate.

1) LOW AND MODERATE WINDS

As shown in Fig. 3, for u_*c^{-1} less than about 2.5 (approximately $U_{10} < 13\text{--}16 \text{ m s}^{-1}$ for the Ku and C band and $U_{10} < 30 \text{ m s}^{-1}$ for L-band Bragg resonance waves described in the last paragraph), the spectrum of a given wavenumber can be approximated by the power-law function $B(u_*c^{-1}; k) = A(k)(u_*c^{-1})^{a(k)}$, with A and a varying with k . Figure 4 shows the results of $A(k)$ and $a(k)$ obtained from fitting the power-law function to the $B(u_*c^{-1}; k)$ inverted from the GMFs in low-to-moderate wind speeds; the data range of u_*c^{-1} used for the least squares fitting is between 0.2 and 2.5. Also included in the figure are the results derived from analyzing the wave spectra measured by free-drifting wave gauges (FDWGs) in the ocean (Hwang and Wang 2004a; Hwang 2008). The roughness spectrum parameterization factors $A(k)$ and

$a(k)$ obtained from in situ and remote sensing data are in close agreement.

Expressing the roughness spectrum as a power-law function of wind speed, the factor $a(k)$ is the wind speed exponent. Many analyses of microwave measurements also yield the equivalent wind speed exponent from fitting the NRCS or brightness temperature measurements (at a given microwave frequency and incidence angle in different wind speeds) to a power-law function of wind speed or wind friction velocity. The results summarized in Fig. 5 of Hwang (1997) and Fig. 4 of Trokhimovski and Irisov (2000) are superimposed in Fig. 4b. Note that there are a lot of radar measurements on the wind speed exponent $a(k)$ but very few published $A(k)$ because calibrated NRCS data are needed for deriving $A(k)$ whereas relative (uncalibrated) measurements are sufficient for deriving $a(k)$. The results from radar “spectrometer” analysis of surface waves as shown in Fig. 4 support the roughness spectrum parameterization presented in Hwang (2005, 2008, 2011) for microwave applications in low-to-moderate wind speeds (u_*c^{-1} less than about 3 or U_{10} less than about $15\text{--}20 \text{ m s}^{-1}$).

2) HIGH WINDS

The roughness spectra in high winds (u_*c^{-1} greater than about 3) derived from the three GMFs tend to converge to the $(u_*c^{-1})^{0.75}$ similarity form (Fig. 3). To extend the roughness spectrum to higher wind speeds,

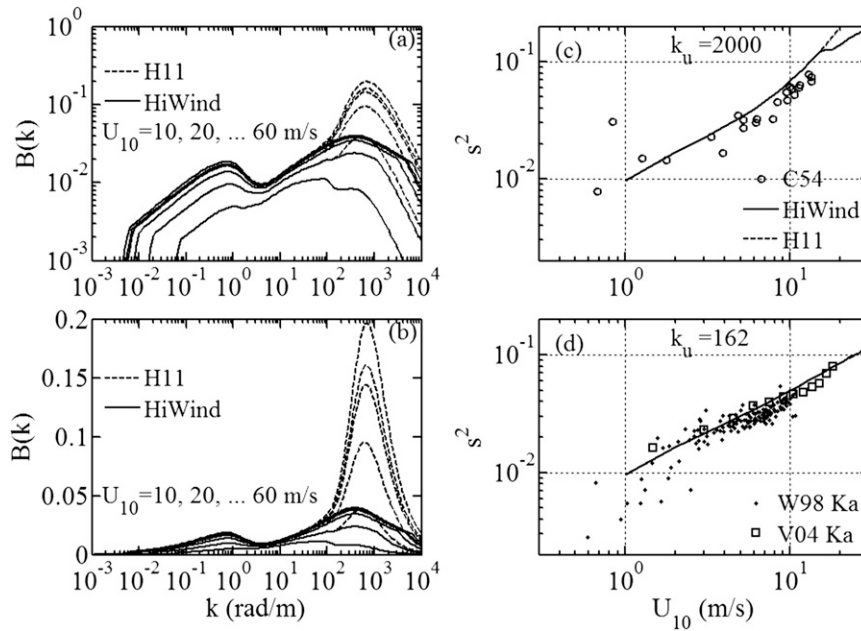


FIG. 5. The roughness spectrum computed with the H11 algorithm and comparison with the high wind modification described in section 3: (a) in log–log scales to show the range and (b) in semilogarithmic scales to show the wavenumber distribution of the mean square slopes. Comparison of the mean square slopes integrated from the roughness spectra with (c) optical data of Cox and Munk (1954; C54) and (d) Ka-band radar data of Walsh et al. (1998; W98) and Vandemark et al. (2004; V04). The upper-bound wavenumber k_u for spectrum integration to obtain the low-passed mean square slopes is shown in each panel.

we may use this observed similarity asymptote behavior. Specifically, the following modification can be implemented for $u_*c^{-1} \geq 3$:

$$\begin{aligned}
 B_h\left(\frac{u_*}{c}; k\right) &= A_h \left(\frac{u_*}{c}\right)^{a_h}, \\
 a_h &= 0.75, \quad \text{and} \\
 A_h &= A_{11}(k_m)(3)^{a_{11}(k_m)-0.75}, \quad (7)
 \end{aligned}$$

where subscript h indicates the quantities for $u_*c^{-1} \geq 3$, and $A_{11}(k_m)$ and $a_{11}(k_m)$ are calculated with the H11 algorithm (see appendix) for the matching wavenumber k_m at $(u_*c^{-1})_m = 3$. As noted earlier, c and k are related by the surface wave dispersion relationship: $c^2 = gk^{-1} + \tau k$.

In the actual implementation, the wave spectra are computed for a range of U_{10} and k based on the H11 algorithm, denoted as $B_{11}(U_{10}, k)$ here. For each wind speed, a search is performed to extract the k components satisfying $u_*c^{-1} \geq 3$, and those $B_{11}(k)$ are substituted by $B_h(k)$ computed with (7). The modification is designed to ensure a smooth transition between the modified high wind roughness spectrum and the H11 algorithm across the full wavenumber range (or u_*c^{-1} range). However,

for short-scale waves influenced by both gravity and capillary forces, the phase speed is not a monotonic function of wavenumber. The extracted components are centered around the critical wavenumber of minimum phase speed: $k_c = g^{0.5}\tau^{-0.5}$, with $g = 9.8 \text{ m s}^{-2}$ and $\tau = 7 \times 10^{-5} \text{ m}^3 \text{ s}^{-2}$, then $k_c = 374 \text{ rad m}^{-1}$. For each wind speed, there may be 0, 1, or 2 matching wavenumbers with $(u_*c^{-1})_m = 3$. In the case of dual matching wavenumbers, the modification (7) is applied to the lower k_m , and this procedure produces a jump in the spectral level at the higher matching wavenumber. The discontinuity is removed by applying a multiplication factor $B_h(k_{m2})/B_{11}(k_{m2})$ to the high wavenumber tail ($k > k_{m2}$), where k_{m2} is the higher matching wavenumber; that is, $B(k) = B_{11}(k)[B_h(k_{m2})/B_{11}(k_{m2})]$ for $k \geq k_{m2}$.

Figure 5a illustrates the comparison of the modified spectra and the H11 results for wind speeds from 10 to 60 m s^{-1} in log–log scales to illustrate the large range of the coverage. The excessive growth of the roughness spectral density in the H11 algorithm is tempered by implementing the high wind switch in (7). Figure 5b replots the spectra in semilogarithmic scales to illustrate the wavenumber distribution of the mean square slope s^2 (Hwang 2005): $s^2|_{k_1}^{k_2} = \int_{k_1}^{k_2} k^2 F(k) dk = \int_{k_1}^{k_2} k^3 F(k) d(\ln k) = \int_{k_1}^{k_2} B(k) d(\ln k)$.

Bandpass-filtered mean square slopes can be generated with the roughness spectrum. The integrated low-pass-filtered mean square slopes from the roughness spectrum are compared with field measurements by an optical (sun glitter) method (Cox and Munk 1954) in Fig. 5c and with microwave results in Fig. 5d; here, the Ka-band data (Walsh et al. 1998; Vandemark et al. 2004) are shown. The wind speed range in the available mean square slope field data is mostly below 20 m s^{-1} , and the effect of the high wind switch in (7) is negligible in such wind speeds. The spectrum-integrated mean square slopes are in good agreement with the optical or microwave measurements. More discussions on the comparison with mean square slopes of multiple frequency bands have been given in Hwang (2008, 2011), Hwang and Plant (2010), and Hwang et al. (2011a).

The mean-square slope integrated from the spectral peak wavenumber k_p to an arbitrary upper-bound wavenumber k_u is denoted by

$$s^2(k_u) = \int_{k_p}^{k_u} k^2 F(k) dk. \tag{8}$$

By varying U_{10} from 2 to 50 m s^{-1} and k_u from 1 to 10^4 rad m^{-1} , a dataset of $s^2(k_u)$ as a function of U_{10} and k_u is created. The wind speed dependence deviates from the empirical linear relationship over the wide range of wind speeds (Fig. 6a) and can be written as

$$s^2(k_u) = b_2(k_u)U_{10}^2 + b_1(k_u)U_{10} + b_0(k_u). \tag{9}$$

Least squares fitting procedure is applied to compute $b_2(k_u)$, $b_1(k_u)$, and $b_0(k_u)$ for wind sea and mixed sea conditions (Hwang 2005, 2008; the appendix). The systematic variations of $b_2(k_u)$, $b_1(k_u)$, and $b_0(k_u)$ shown in Fig. 6b can be represented by the following polynomial functions of $k_{\ln} = \ln(k_u)$:

$$\begin{aligned}
 b_2 &= \begin{cases} 6.54 \times 10^{-9}k_{\ln}^5 - 5.30 \times 10^{-8}k_{\ln}^4 - 3.50 \times 10^{-7}k_{\ln}^3 + 2.26 \times 10^{-6}k_{\ln}^2 \\ \quad - 6.59 \times 10^{-6}k_{\ln} - 9.41 \times 10^{-6} & \text{for wind sea} \\ 8.39 \times 10^{-9}k_{\ln}^5 - 9.00 \times 10^{-8}k_{\ln}^4 - 1.59 \times 10^{-7}k_{\ln}^3 + 2.42 \times 10^{-6}k_{\ln}^2 \\ \quad - 7.66 \times 10^{-6}k_{\ln} - 8.14 \times 10^{-6} & \text{for mixed sea} \end{cases} \\
 b_1 &= \begin{cases} -5.80 \times 10^{-9}k_{\ln}^5 - 7.77 \times 10^{-6}k_{\ln}^4 + 1.27 \times 10^{-4}k_{\ln}^3 - 5.00 \times 10^{-4}k_{\ln}^2 \\ \quad + 9.64 \times 10^{-4}k_{\ln} + 1.64 \times 10^{-3} & \text{for wind sea} \\ -4.41 \times 10^{-7}k_{\ln}^5 + 1.15 \times 10^{-6}k_{\ln}^4 + 7.58 \times 10^{-5}k_{\ln}^3 - 4.82 \times 10^{-4}k_{\ln}^2 \\ \quad + 1.15 \times 10^{-3}k_{\ln} + 1.61 \times 10^{-3} & \text{for mixed sea} \end{cases}, \text{ and} \\
 b_0 &= \begin{cases} -2.05 \times 10^{-6}k_{\ln}^6 + 5.74 \times 10^{-5}k_{\ln}^5 - 5.51 \times 10^{-4}k_{\ln}^4 + 1.94 \times 10^{-3}k_{\ln}^3 - 1.50 \times 10^{-3}k_{\ln}^2 \\ \quad + 7.36 \times 10^{-4}k_{\ln} - 5.88 \times 10^{-3} & \text{for wind sea} \\ -3.11 \times 10^{-6}k_{\ln}^6 + 8.98 \times 10^{-5}k_{\ln}^5 - 9.09 \times 10^{-4}k_{\ln}^4 + 3.60 \times 10^{-3}k_{\ln}^3 - 3.96 \times 10^{-3}k_{\ln}^2 \\ \quad + 1.15 \times 10^{-3}k_{\ln} - 6.50 \times 10^{-3} & \text{for mixed sea} \end{cases}. \tag{10}
 \end{aligned}$$

Here, (10) can be used to calculate the mean-square slope of an arbitrary wavenumber band of the ocean surface roughness.

4. Verification of the roughness spectrum model

a. Radar backscatter comparison

A comprehensive dataset of short-wave spectra obtained with conventional wave measuring techniques does not exist, thus a direct verification of the proposed roughness spectrum model with field data is not feasible at the present. As mentioned earlier, the radar backscatter is strongly influenced by the ocean surface roughness in the Bragg resonance scales. One way of

evaluating the roughness spectrum model is to compare the NRCS computation using the modeled roughness spectrum with the radar measurement. A known issue of the H11 algorithm lies in the high wind region: scatterometer observations show a saturation trend (e.g., Donnelly et al. 1999) but the NRCS computation using the H11 roughness spectrum continues to increase. The discrepancy between the scatterometer GMF and the NRCS computation in high wind increases toward higher incidence angle and higher microwave frequency (see, e.g., Fig. 2 of Hwang 2011).

Figure 7 shows the NRCS computations for the VV polarization using the roughness spectrum with and without the high wind switch in (7) covering wind speeds up to 60 m s^{-1} and their comparison with the Ku-, C-,

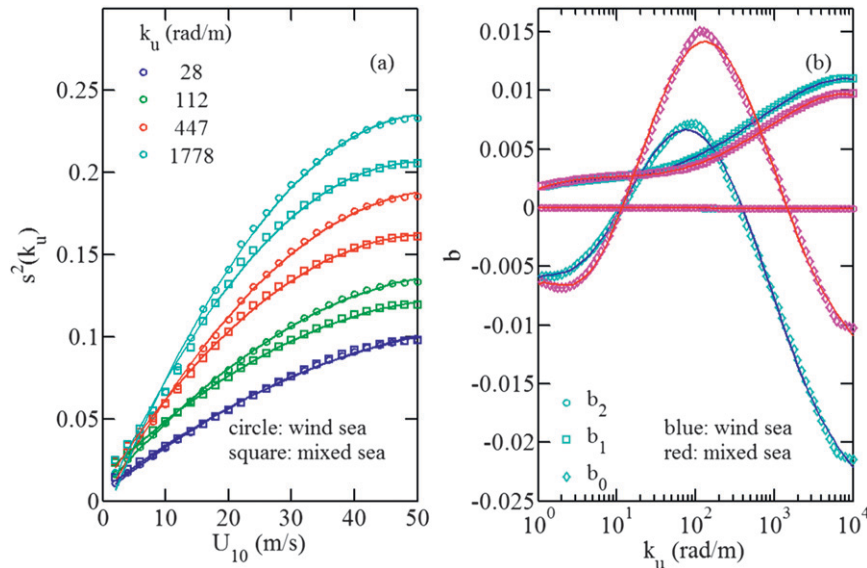


FIG. 6. (a) Mean square slopes integrated from k_p to k_u ; examples of 4 values of k_u are plotted as a function of wind speed: circles show wind sea and squares for mixed sea with moderate swell. The second-order polynomial fitting curves are plotted with solid lines. (b) The coefficients of the second-order polynomial fitting functions b_2 , b_1 , and b_0 plotted as a function of k_u , and their fitted curves are represented by (9).

and L-band GMFs. The trend of decreasing wind speed sensitivity toward higher wind is improved in the computed NRCS using the roughness spectrum with the high wind switch. The effect is especially obvious for the Ku band. The impact of the high wind switch on the C-band computation is somewhat reduced, and no impact is

expected for the L-band computation. This is caused mainly by the smaller difference between 0.75 (the wind speed exponent of the high wind switch) and the wind speed exponents of the Bragg resonance wave components over the low and medium wind speeds in C and L bands compared to that in the Ku band (Figs. 3a and 4b).

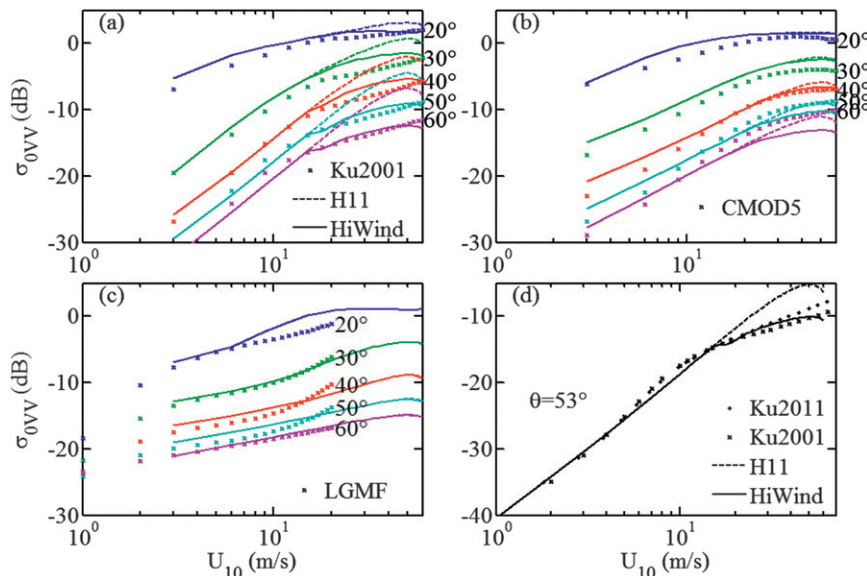


FIG. 7. Comparison of the $\sigma_{0VV}(\theta)$ computed with the H spectrum with (a) Ku-, (b) C-, and (c) L-band GMFs for $\theta = 20^\circ$ – 60° , and (d) Ku2001 and Ku2011 GMFs for $\theta = 53^\circ$. Dashed curves show computations with the H11 algorithm without the high wind switch in (7), and solid curves are computations with the high wind switch applied.

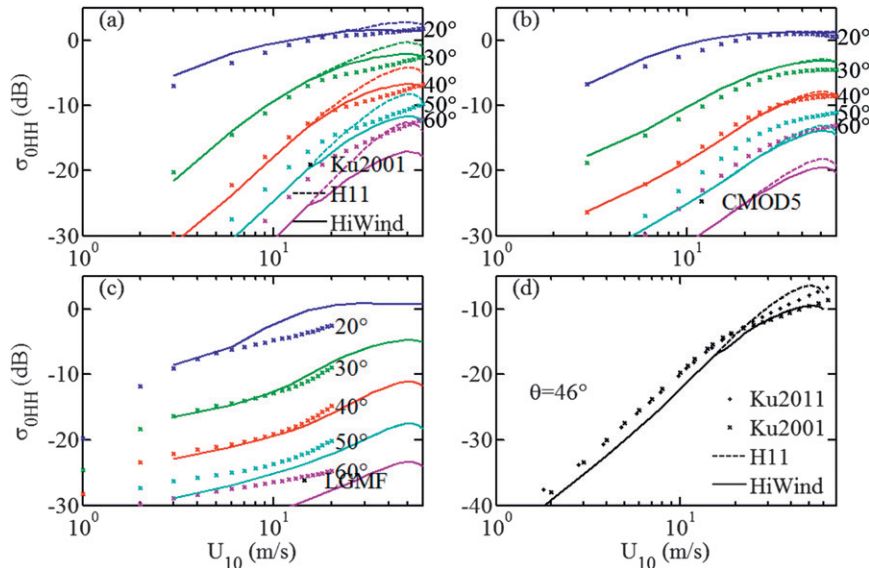


FIG. 8. As in Fig. 7, but for $\sigma_{0HH}(\theta)$ and in (d) Ku2001 and Ku2011 GMFs for $\theta = 46^\circ$.

Recently, Ricciardulli and Wentz (2011) present a new Ku-band GMF: the Ku2011, which expresses the NRCS in six cosine harmonic terms of the azimuthal angle for each wind speed from 0 to 70 m s^{-1} in steps of 0.2 m s^{-1} . They show that compared to the Ku2001 wind velocity retrieval, the Ku2011 yields significant improvement in the Quick Scatterometer (QuikSCAT) high wind measurements (Ricciardulli et al. 2012). The Ku2011 is given for one incident angle of each polarization (46° for HH and 53° for VV). Figure 7d compares the two Ku-band GMFs and the NRCS computations using the H11 roughness spectrum with and without the high wind switch [(7)]. The application of the high wind switch clearly improves the agreement between the calculated NRCS and Ku2011 for U_{10} up to about 40 m s^{-1} . The subsequent decrease of the calculated NRCS for $U_{10} > 40 \text{ m s}^{-1}$ is not observed in the Ku2011 or Ku2001 GMF. The decrease in the calculated NRCS is caused by the u_* reduction above 50 m s^{-1} wind speed as a consequence of the drag coefficient in (2). This result indicates that the uncertainty of the drag coefficient in high wind conditions remains to be resolved; further discussion is given in section 5b.

Figure 8 shows the NRCS computations for the HH polarization. The wind speed and incidence angle ranges are identical to those in Fig. 7, except for Fig. 7d in which $\theta = 46^\circ$. The NRCS computation is in good agreement with the GMFs for θ less than or equal to about 40° . For steeper incidence angles, the backscatter computation is a few decibels too small and indicates that the contribution from sea spikes associated with steep or breaking waves becomes increasingly important for the HH

polarization toward higher incidence angles (e.g., Hwang et al. 2008 and references therein).

b. Radiometer brightness temperature comparison

Another remote sensing data source for verifying the roughness spectrum model performance is the brightness temperature output of passive microwave radiometers. Hwang (2012) presents numerical simulations of foam and roughness effects on the brightness temperature using the H11 roughness spectrum and an empirical model of whitecap coverage. The results are compared with a global dataset of WindSat measurements with wind speed coverage up to about 42 m s^{-1} (Meissner and Wentz 2009). The WindSat data include five microwave frequencies (6, 10, 18, 23, and 37 GHz) for both vertical and horizontal polarizations. The agreement between simulation and measurement is generally very good up to about either 20 or 25 m s^{-1} (frequency dependent). In higher wind speeds the simulated wind effects exceed observations. We have repeated the numerical simulation using the same H11 roughness spectrum but with the high wind switch in (7). Figure 9 shows the result; the agreement with WindSat data is improved with the high wind switch applied.

5. Discussion

a. Mean square slope distribution in wavenumber space

As described in section 2, the H roughness spectrum seeks to produce a better parameterization in the spectral band with a strong contribution to the ocean surface

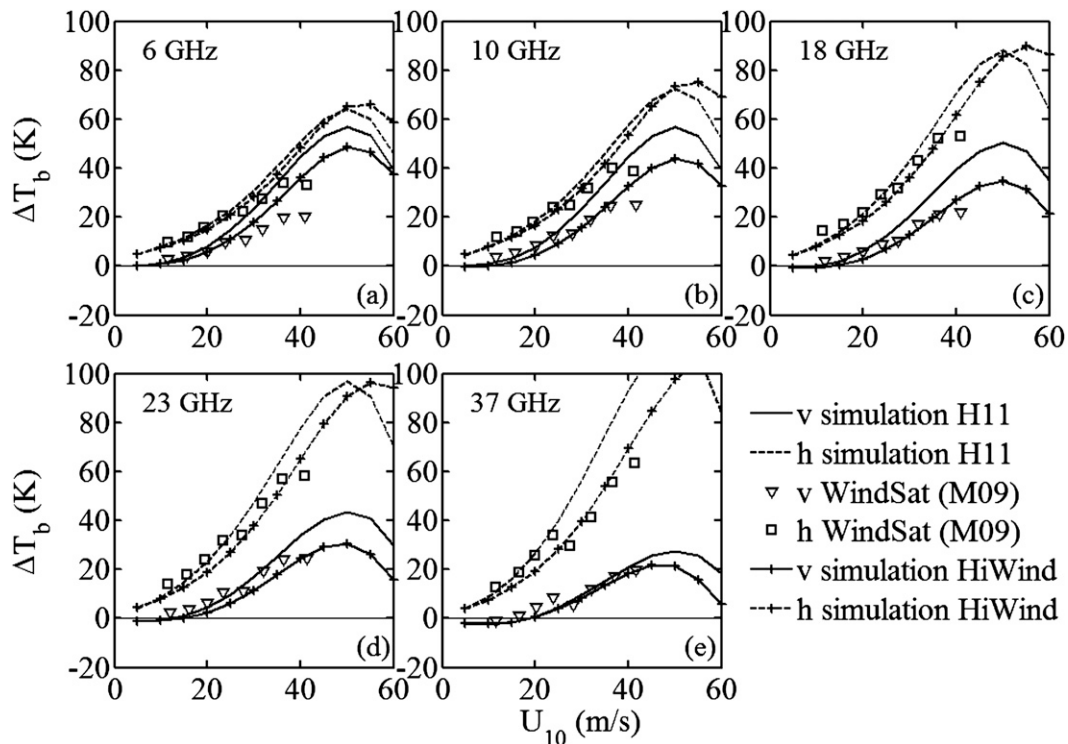


FIG. 9. Wind modification of the brightness temperature due to foam and roughness effects at five microwave frequencies calculated with the H11 algorithm with and without the high wind switch and comparison with the global WindSat data reported by Meissner and Wentz (2009; M09).

mean square slope, and relatively simple asymptote functions are used for the extension of the roughness spectrum model into both higher and lower wavenumber ends of the model coverage (Hwang 2008, 2011). It is for this reason we have used the term roughness spectrum instead of the wave spectrum that generally emphasizes the energy-containing portion of the ocean surface waves.

Of special concern is that toward the low wavenumber end, an equilibrium asymptote is assumed to extend to the peak wavenumber defined as $k_p = \omega_{\#}^2 g U_{10}^{-2}$, where the dimensionless wave spectrum peak frequency $\omega_{\#}$ is the inverse wave age for deep water waves (appendix). For $\omega_{\#} = 1$ employed in this paper, the corresponding peak wave period is $T_p = 2\pi U_{10} g^{-1}$. When the spectrum model application is expanded to very high wind speed, the calculated peak wave period becomes unrealistically long. For example, at $U_{10} = 20, 40,$ and 60 m s^{-1} , $T_p = 12.8, 25.6,$ and 38.5 s . Because high wind events are generally associated with moving storm systems, the effective duration and fetch for wind wave generation is usually less than the limiting condition. Field observations show that peak wave periods rarely exceed 20 s (e.g., Wright et al. 2001; Jonathan et al. 2010). It is

therefore of some concern about overspecifying the long-scale waves in the H roughness spectrum.

Figure 10a shows the mean square slopes cumulated from k_p to k_u [(8)] of the roughness spectra displayed in Fig. 5. The circle on each curve indicates k_p for the given wind speed. It is clear that the contribution of mean square slope from long waves near the spectrum peak is rather small. In fact, the integration from k_p to $2k_p$ (or $3k_p$ for very high winds) remains below the ambient level of mean square slopes in field observations: the dotted curve represents the ambient level of 3×10^{-3} in the data of Cox and Munk (1954). Examination of the altimeter NRCS data suggests an even higher ambient level (about 0.02) of the mean square slope in the ocean (Hwang et al. 1998). In the figure, we also show the representative Bragg wavenumbers for the L, C, and Ku band (calculated with 1, 6, and 14 GHz at a 45° incidence angle). As wind speed increases, the spectral peak moves further away from the Bragg region: the neighborhood of the Bragg region represents the most critical spectral band concerning microwave scatterometer and radiometer computations.

Figure 10b shows the cumulative mean square slopes derived from three frequently referenced wind sea

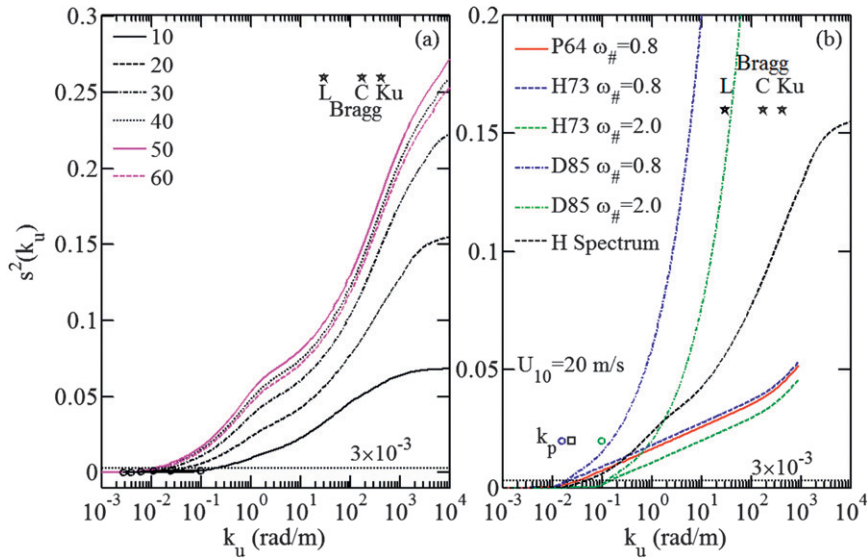


FIG. 10. (a) The cumulative mean square slopes integrated from k_p to k_u of the roughness spectra displayed in Fig. 5; here k_p , shown with a circle in each curve, is defined as $k_p = \omega_{\#}^2 g / U_{10}^2$ and the inverse wave age $\omega_{\#}$ is 1 in this example. The representative Bragg resonance wavenumbers for L-, C-, and Ku-band frequencies are plotted with stars, and the ambient level of mean square slopes (3×10^{-3}) observed in the ocean data of Cox and Munk (1954) is shown with a dotted line. (b) Comparison of the cumulative mean square slopes of the H roughness spectrum at $U_{10} = 20 \text{ m s}^{-1}$ with those obtained from three popular wind sea spectrum models, PM (P64), JONSWAP (H73), and Donelan (D85) at two different wave ages; see text for further detail.

spectrum models: PM (Pierson and Moskowitz 1964), JONSWAP (Hasselmann et al. 1973), and Donelan (Donelan et al. 1985). The wind speed is 20 m s^{-1} and the upper frequency is set at a rather high 40 Hz for the purpose of illustration. The result based on the H spectrum (with high wind switch on) is also displayed for comparison. The PM is designed for the fully developed sea, represented by the inverse wave age $U_{10}/c_p = \omega_{\#} = 0.8$, whereas JONSWAP and Donelan consider wave age as a separate parameter, illustrated in the figure for $\omega_{\#} = 0.8$ and 2.0. The H spectrum is computed for $\omega_{\#} = 1.0$.

The main difference in the short-wave portion of the three popular wind wave models is the 1D spectral slope (in the gravity wave region): f^{-5} or k^{-3} for the PM and JONSWAP models, corresponding to the saturation spectrum of Phillips (1958), and f^{-4} or $k^{-2.5}$ for the Donelan model, corresponding to the equilibrium spectrum of Phillips (1985). The mean square slopes derived from a spectrum with a $k^{-2.5}$ high-frequency tail is, of course, unlimited and increases rapidly with the upper range of the integration wavenumber. This is manifested in the cumulative mean square slope curves based on the Donelan spectrum model (Fig. 10b). In contrast, the mean square slope integrated from the saturation spectrum model with k^{-3} high-frequency tail increases

logarithmically with wind speed, which is less than the quasi-linear dependence observed in the field data (e.g., Cox and Munk 1954). See also discussions in sections 3 and 5 of Hwang and Wang (2001). It is obvious that the equilibrium range (with $k^{-2.5}$ dependence) must be of a finite spectral width to avoid an explosion of the integrated mean square slope. With comparison to field observations of the mean square slopes and a consideration of the wavenumber components participated in the nonlinear wave-wave interaction, Hwang and Wang (2001, p. 1349) estimate that the width of the equilibrium spectrum is about $(2.5 \pm 0.5) \omega_p$ or $(6.5 \pm 2) k_p$.

The result based on the H spectrum is somewhere between those of the three wind wave spectrum models in the low wavenumber region (Fig. 10b), and the mean square slope integration is convergent: the high wavenumber asymptote is $B(k) \sim (u_* c^{-1})^3 \sim k^{-1.5}$ using the dispersion relationship of capillary waves $c^2 = \tau k$, so the high wavenumber asymptote of the slope spectrum is $k^2 F(k) = k^{-1} B(k) \sim k^{-2.5}$.

b. Drag coefficient

The study of the ocean surface drag coefficient is of great interest to a wide range of research areas, including wave dynamics, air-sea interaction, weather and

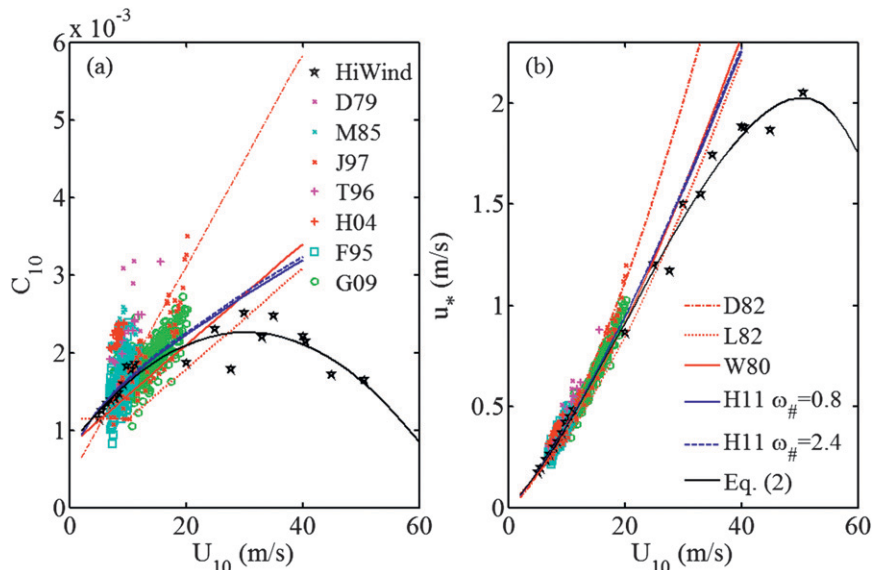


FIG. 11. Parameterization of the ocean surface drag coefficient in terms of $C_{10}(U_{10})$ for (a) seven field datasets: Donelan (1979; D79), Merzi and Graf (1985; M85), Janssen (1997; J97), Terray et al. (1996; T96), Hwang and Wang (2004b; H04), Felizardo and Melville (1995; F95), and García-Nava et al. (2009; G09), and (b) three published formulas: Wu (1980; W80), Donelan (1982; D82), and Large and Pond (1982; L82) shown in color. The open ocean data used in Fig. 1 and the fitted curve (2) are shown in black.

climate, and ocean remote sensing. Wind speed, air and water temperatures, and surface wave conditions are among the many factors influencing the magnitude of the ocean surface drag coefficient. Under neutral stratification or after air–sea stability correction, the ocean surface drag coefficient varies with wind speed and surface wave conditions in a rather complex fashion. Many empirical formulas have been published (e.g., Wu 1980; Donelan 1990; Geernaert 1990). In the absence of surface wave information, the drag coefficient is frequently expressed as a linear function of U_{10} :

$$C_{10} = K_0 + K_1 U_{10}, \quad (11)$$

where K_0 and K_1 are the regression coefficients obtained from fitting to experimental data. Table 1 of Geernaert (1990) lists 28 different formulas. Figure 11a shows the upper and lower ranges among the 28 curves. The upper bound is Donelan (1982), $[K_0, K_1] = [0.37 \times 10^{-3}, 0.137 \times 10^{-3}]$ and the lower bound is Large and Pond (1982), $[K_0, K_1] = [1.14 \times 10^{-3}, 0]$ for $4 \leq U_{10} < 10 \text{ m s}^{-1}$ and $[0.49 \times 10^{-3}, 0.065 \times 10^{-3}]$ for $10 \leq U_{10} < 26 \text{ m s}^{-1}$. Also shown is the formula of Wu (1980) obtained from averaging 33 independent field datasets $[K_0, K_1] = [0.8 \times 10^{-3}, 0.065 \times 10^{-3}]$; this formula is used in the third generation wave model (WAMDI group 1988)

with a slight modification: $[K_0, K_1] = [1.2875 \times 10^{-3}, 0]$ for $U_{10} < 7.5 \text{ m s}^{-1}$ and $[0.8 \times 10^{-3}, 0.065 \times 10^{-3}]$ for $U_{10} \geq 7.5 \text{ m s}^{-1}$.

Superimposed in the figure are seven field datasets: five are wind seas with presumably single-peaked surface wave spectra (Donelan 1979; Merzi and Graf 1985; Janssen 1997; Terray et al. 1996; Hwang and Wang 2004b), and two are mixed seas with prominent bimodal or multimodal wave spectra (Felizardo and Melville 1995; García-Nava et al. 2009). The large variation of the experimental data in terms of $C_{10}(U_{10})$ is a clear indication of the surface wave influence that cannot be accounted for by wind speed alone. In the absence of wave information, the divergence of u_* estimation using different drag coefficient functions increases toward higher wind speed (Fig. 11b). In section 2, an empirical function (2) is derived from least squares fitting applied to three open ocean datasets covering low-to-high wind conditions. The empirical function and the data are also shown in Fig. 11. Noticeably, the contrast between different drag coefficient formulas is less dramatic in $u_*(U_{10})$ than in $C_{10}(U_{10})$ because u_* is the product of U_{10} and square root of C_{10} . This is especially obvious in lower wind speeds.

There remains considerable uncertainty on the drag coefficient dependence on wind speed in high winds. The uncertainty obviously impacts the radar backscatter

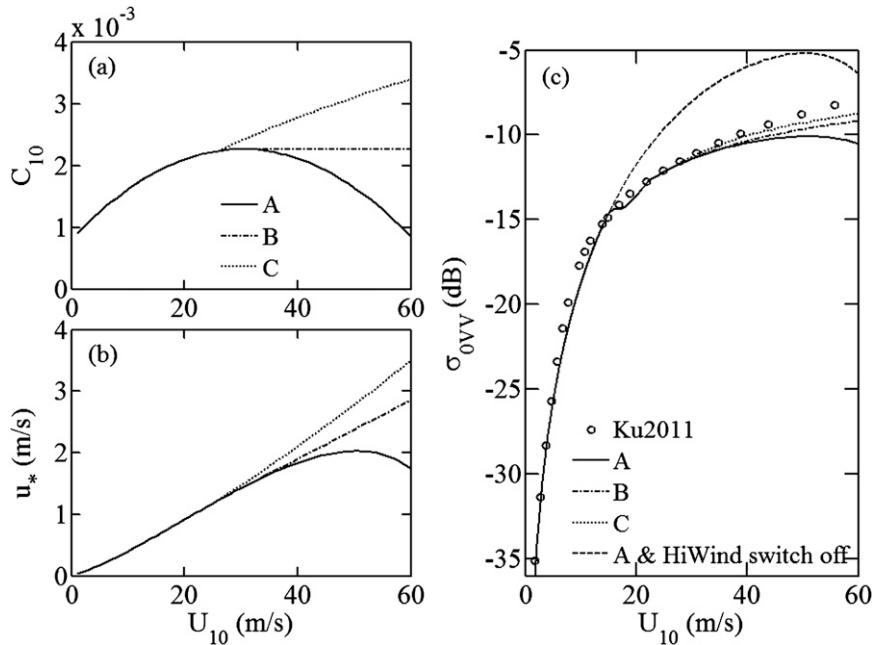


FIG. 12. Examples showing the effect of the drag coefficient on radar NRCS computation: (a) three different variations of C_{10} dependence on U_{10} , (b) the corresponding dependence on u_* , and (c) the resulting $\sigma_{0VV}(U_{10})$ calculated for the Ku2011 GMF condition ($\theta = 53^\circ$) with high wind switch in (7) applied. The NRCS computation with the C_{10} function A but without the high wind switch is also shown for reference.

computations because the roughness is determined by the factor u_*c^{-1} . Figure 12a shows the wind speed function of C_{10} given by (2) and two variations in the high wind region such that C_{10} either remains constant or increases with $U_{10}^{0.5}$ beyond some transition wind speed; the three curves are identified as A, B, and C, respectively. The two variations are formulated by substituting the high wind segment ($U_{10} > U_t$, U_t is a transition wind speed) of the C_{10} curve with $C_{10t}(U_{10}U_t^{-1})^\alpha$, where C_{10t} is C_{10} at U_t . For curve B, $U_t = 25 \text{ m s}^{-1}$ and $\alpha = 0$, and for curve C, $U_t = 30 \text{ m s}^{-1}$ and $\alpha = 0.5$. Figure 12b shows the corresponding u_* . Figure 12c is an example of the computed σ_{0VV} with the high wind switch in (7) applied and its comparison with the Ku2011 GMF. The results indicate that if u_* is a monotonic function of U_{10} , then the σ_{0VV} dependence on U_{10} is also monotonic. Also displayed in Fig. 12c is the computed σ_{0VV} using drag coefficient for A and the high wind switch in (7) turned off. It is clear that the impact of the functional dependence of $B(u_*c^{-1}; k) = A(k)(u_*c^{-1})^{a(k)}$, which is modified in the high wind switch, is generally more significant than the impact produced by using different drag coefficient functions.

At the present, there are only limited data on radar backscatter measurements in high winds. Donnelly et al. (1999) report airborne measurements with C- and

Ku-band scatterometers. The maximum wind speed for the C-band data is about 43 m s^{-1} . The data show that near $25\text{--}30 \text{ m s}^{-1}$ the backscatter intensity seems to saturate and may decrease in higher winds for θ less than about 33° . A similar trend is found in the Ku band, but the wind speed coverage in the dataset is limited to less than about 35 m s^{-1} and the data scatter is quite large. The Ku2011 GMF incorporates many more high wind events from combining 7 yr of QuikSCAT NRCS with vector winds retrieved by the WindSat polarimetric radiometers (Ricciardulli and Wentz 2011). As mentioned in section 4a, the Ku2011 GMF is given for one incident angle of each polarization (46° for HH and 53° for VV). With the continuous improvement in analysis and data accumulation, the remote sensing radar backscatter measurements may prove to be very useful for addressing issues regarding the drag coefficient in high wind conditions.

6. Summary

The source function analysis of Phillips (1984) calls for investigating the functional dependence of the dimensionless short-wave spectrum on the dimensionless wind friction velocity: $B(u_*c^{-1})$. An empirical power-law relationship $B(u_*c^{-1}; k) = A(k)(u_*c^{-1})^{a(k)}$ has been

established with field data obtained in low-to-moderate winds ($2\text{--}14\text{ m s}^{-1}$) covering the wavenumber range between 1 and 300 rad m^{-1} (Hwang and Wang 2004a). This similarity relationship serves as a parameterization function of the ocean surface roughness spectrum (Hwang 2005). To extend the wavenumber coverage, asymptotic functions for the factors $A(k)$ and $a(k)$ are established toward the low wavenumber using our understanding of the equilibrium spectrum of wind-generated waves and toward the high wavenumber using empirical measurements of the wind speed dependence of the radar backscattering cross section (Hwang 2008, 2011). To extend the wind speed coverage, we explore the rich resources of the airborne and spaceborne NRCS measurements. Over the years, Ku-, C-, and L-band GMFs have been refined using the extensive scatterometer observations. As outlined in section 3, the scatterometer serves as a spectrometer of the ocean surface roughness. Combining the three GMFs, the inverted roughness spectra cover the wavenumber range between 31 and 508 rad m^{-1} . More significantly, the wind speed coverage of the global scatterometer measurements includes stormy conditions.

The roughness spectra of the Bragg resonance wave components inverted from the scatterometer measurements fit the similarity function $B(u_*c^{-1}; k) = A(k)(u_*c^{-1})^{a(k)}$ established from in situ short-wave data. For low-to-moderate wind speed range, the parameterization factors $A(k)$ and $a(k)$ derived from scatterometer GMFs are in good agreement with those obtained from in situ surface wave measurements. In high wind condition ($u_*c^{-1} \geq 3$), $B(u_*c^{-1})$ from the three GMFs converge to a common functional form $(u_*c^{-1})^{0.75}$. A relatively minor modification in (7) of the H11 algorithm extends the application range of the roughness spectrum model to high winds. Considerable improvements in the active and passive microwave computations of NRCS and brightness temperature in high winds are achieved with the modification (section 4).

Acknowledgments. This work is sponsored by the Office of Naval Research as part of the projects Sea Surface Roughness Impacts on Microwave Sea Surface Salinity Measurements (SRIMS) and Breaking-Wave Effects under High Winds (BWE). The data for the lookup tables of Ku2001 GMF are provided by Debora Smith, and the cosine harmonic coefficients of Ku2011 GMF are provided by Lucrezia Ricciardulli, both at Remote Sensing Systems. The original SSA/SPM model code used for the radiometer brightness temperature computations is provided by Nicolas Reul (Institut Français de Recherche pour l'Exploitation de la Mer,

France). We are grateful for the comments and suggestions from two anonymous reviewers.

APPENDIX

The H11 Algorithm and Modifications near the Wave Energy Spectrum Peak

The parameters $A(k)$ and $a(k)$ are given in three wavenumber branches: $0 < k \leq k_1$, $k_1 < k \leq k_2$, and $k_2 < k \leq \infty\text{ rad m}^{-1}$, where $k_1 = 1.5$ and $k_2 = 100\text{ rad m}^{-1}$ (Hwang 2011). Simple analytical functions are developed for each branch:

- (i) $A(k)$ and $a(k)$ are expressed as fifth-order polynomial fitting functions of $k_{\ln} = \ln(k)$ for the middle branch $k_1 < k \leq k_2$,

$$\begin{aligned} A(k) &= -3.862 \times 10^{-5} k_{\ln}^5 + 7.991 \times 10^{-4} k_{\ln}^4 \\ &\quad - 6.417 \times 10^{-3} k_{\ln}^3 + 2.342 \times 10^{-2} k_{\ln}^2 \\ &\quad - 3.668 \times 10^{-2} k_{\ln} + 2.898 \times 10^{-2} \quad \text{and} \\ a(k) &= -5.213 \times 10^{-4} k_{\ln}^5 + 1.524 \times 10^{-2} k_{\ln}^4 \\ &\quad - 1.358 \times 10^{-1} k_{\ln}^3 + 5.865 \times 10^{-1} k_{\ln}^2 \\ &\quad - 1.167 k_{\ln} + 1.136. \end{aligned} \quad (\text{A1})$$

- (ii) The terms $A(k)$ and $a(k)$ approach asymptotically to the low-frequency limits of $A_0 = 5.2 \times 10^{-2}$ and $a_0 = 1$ in the low wavenumber range $0 < k \leq k_1$,

$$\begin{aligned} A(k) &= A_0 \exp\left\{ \frac{k}{k_1} \left[\ln \frac{A(k_1)}{A_0} \right] \right\} = A_0 \left[\frac{A(k_1)}{A_0} \right]^{k/k_1} \\ \text{and} \\ a(k) &= a_0 \exp\left\{ \frac{k}{k_1} \left[\ln \frac{a(k_1)}{a_0} \right] \right\} = a_0 \left[\frac{a(k_1)}{a_0} \right]^{k/k_1}. \end{aligned} \quad (\text{A2})$$

The terms $A(k_1)$ and $a(k_1)$ are computed with (A1) to maintain continuity with the middle branch. The selection of asymptotic values for A_0 and a_0 are based on the extensive research results on the coefficient and exponent of the power-law wind speed dependence of the wind wave spectrum, as discussed in section 2 of Hwang (2008).

- (iii) The terms $A(k)$ and $a(k)$ approach asymptotically to the high-frequency limits of $A_\infty = 2 \times 10^{-3}$ and $a_\infty = 2.5$ or $A_\infty = 10^{-3}$ and $a_\infty = 3$ in the high wavenumber range $k_2 < k \leq \infty$,

TABLE A1. Coefficients of the polynomial fitting equation $Y = \sum_{n=0}^N P_n [\ln(k)]^n$ and Y is the parameter shown in the first column for mild (B), moderate (C), and high (D) swell conditions.

	P_5	P_4	P_3	P_2	P_1	P_0
R_A (B)	2.811×10^{-3}	-4.911×10^{-2}	3.040×10^{-1}	-7.542×10^{-1}	5.349×10^{-1}	1.159×10^0
R_a (B)	1.127×10^{-2}	-1.948×10^{-1}	1.241×10^0	-3.443×10^0	3.683×10^0	-3.779×10^{-2}
R_A (C)	4.258×10^{-3}	-7.628×10^{-2}	4.905×10^{-1}	-1.310×10^0	1.176×10^0	1.049×10^0
R_a (C)	9.373×10^{-3}	-1.645×10^{-1}	1.057×10^0	-2.907×10^0	2.855×10^0	4.543×10^{-1}
R_A (D)	-2.318×10^{-3}	4.107×10^{-2}	-3.092×10^{-1}	1.278×10^0	-2.769×10^0	3.024×10^0
R_a (D)	1.384×10^{-2}	-2.394×10^{-1}	1.512×10^0	-4.019×10^0	3.569×10^0	3.932×10^{-1}

$$A(k) = A_\infty \exp\left\{\frac{k_2}{k} \left[\ln \frac{A(k_2)}{A_\infty}\right]\right\} = A_\infty \left[\frac{A(k_2)}{A_\infty}\right]^{k_2/k}$$

$$F_p(k) = \gamma^{\exp\{[-(k-k_p)]/2\sigma^2 k_p\}}, \quad \text{where } \sigma = \begin{cases} \sigma_1, & k < k_p \\ \sigma_2, & k \geq k_p \end{cases} \quad (\text{A5})$$

and

$$a(k) = a_\infty \exp\left\{\frac{k_2}{k} \left[\ln \frac{a(k_2)}{a_\infty}\right]\right\} = a_\infty \left[\frac{a(k_2)}{a_\infty}\right]^{k_2/k} \quad (\text{A3})$$

Numerical simulations of NRCS based on the two sets of (A_∞, a_∞) produce similar outcomes. The results given in this paper are based on the first set ($A_\infty = 2 \times 10^{-3}$ and $a_\infty = 2.5$). The terms $A(k_2)$ and $a(k_2)$ are computed with (A1) to maintain continuity with the middle branch. The choice of a_∞ value is based on the numerous measurements of the wind speed dependence of microwave radar cross sections at different incidence angles and various microwave frequencies. The choice of A_∞ is from comparing the NRCS computation with the Ku- and C-band GMFs.

The (inverse) wave age parameter $\omega_\# = \omega_p U_{10}/g$, which is U_{10}/c_p for the deep water wave condition, can be introduced in the low wavenumber branch (ii) by setting $B(k)$ to 0 for the wavenumber components satisfying $k < k_p$, where $k_p = \omega_\#^2 g/U_{10}^2$. Alternatively, a smooth transition can be achieved by multiplying the computed $B(k)$ with a Gaussian shape function designed in a similar fashion of the Pierson–Moskowitz spectrum (Pierson and Moskowitz 1964):

$$F_G = \begin{cases} \exp\left[-\left(\frac{k_p}{k}\right)^2 - 1\right], & k < k_p \\ 1, & k \geq k_p \end{cases} \quad (\text{A4})$$

The peak enhancement factor that is an important feature of nonlinear wave–wave interaction in the JONSWAP spectrum (Hasselmann et al. 1973) can also be incorporated:

From field experiments, the mean values of γ and σ are about 3 and 0.1, respectively; the difference between σ_1 and σ_2 is small (Hasselmann et al. 1973, Fig. 2.8). Although these peak modifications are important feature of the wind wave energy spectrum, their influence on microwave backscatter and brightness temperature computations is negligible. The results presented in this paper is computed for $\omega_\# = 1$.

The swell influence is introduced by the modification factors derived from field data: $R_A(k) = A_{\text{swell}}(k)/A_{\text{windsea}}(k)$ and $R_a(k) = a_{\text{swell}}(k)/a_{\text{windsea}}(k)$, expressed as fifth-order polynomial functions [Table A1, reproduced from Table 1 of Hwang (2008)]. The swell intensity is qualitatively divided into B, C, and D categories for mild, moderate, and high based on the available short-wave spectrum data reported in Hwang and Wang (2004a) and Hwang (2008). Category A is the reference wind sea condition with $R_A = R_a = 1$.

REFERENCES

Apel, R. J., 1994: An improved model of the ocean surface wave vector spectrum and its effects on radar backscatter. *J. Geophys. Res.*, **99** (C8), 16 269–16 290.

Banner, M. L., 1990: Equilibrium spectra of wind waves. *J. Phys. Oceanogr.*, **20**, 966–984.

—, I. S. F. Jones, and J. C. Trinder, 1989: Wavenumber spectra of short gravity waves. *J. Fluid Mech.*, **198**, 321–344.

Bjerkaas, A. W., and F. W. Riedel, 1979: Proposed model for the elevation spectrum of a wind-roughened sea surface. Johns Hopkins University Applied Physics Laboratory Tech. Memo. TG 1328, 32 pp.

Bock, E. J., and T. Hara, 1995: Optical measurements of capillary-gravity wave spectra using a scanning laser slope gauge. *J. Atmos. Oceanic Technol.*, **12**, 395–403.

Br on, F. M., and N. Henriot, 2006: Spaceborne observations of ocean glint reflectance and modeling of wave slope distributions. *J. Geophys. Res.*, **111**, C06005, doi:10.1029/2005JC003343.

Caponi, E. A., D. R. Crawford, H. C. Yuen, and P. G. Saffman, 1988: Modulation of radar backscatter from the ocean by

- a variable surface current. *J. Geophys. Res.*, **93** (C10), 12249–12263.
- Chaudhry, A. H., and R. K. Moore, 1984: Tower-based backscatter measurements of the sea. *IEEE J. Oceanic Eng.*, **9**, 309–316.
- Cox, C. S., 1958: Measurements of slopes of high-frequency wind waves. *J. Mar. Res.*, **16**, 198–223.
- , and W. Munk, 1954: Statistics of the sea surface derived from sun glitter. *J. Mar. Res.*, **13**, 198–227.
- Crombie, D. D., 1955: Doppler spectrum of sea echo at 13–56 Mc/s. *Nature*, **175**, 681–682.
- Dias, F., and C. Kharif, 1999: Nonlinear gravity and capillary-gravity waves. *Annu. Rev. Fluid Mech.*, **31**, 301–346.
- Donelan, M. A., 1979: On the fraction of wind momentum retained by waves. *Mar. Forecasting*, J. C. J. Nihoul, Ed., Elsevier, 141–159.
- , 1982: The dependence of the aerodynamic drag coefficient on wave parameters. Preprints, *First Int. Conf. on Meteorology and Air–Sea Interaction*, The Hague, Netherlands, Amer. Meteor. Soc., 381–387.
- , 1990: Air–sea interaction. *The Sea*, B. LeMehaute and D. M. Hanes, Eds., *Ocean Engineering Science*, Vol. 9, John Wiley and Sons, 239–292.
- , and W. J. Pierson, 1987: Radar scattering and equilibrium ranges in wind-generated waves with application to scatterometry. *J. Geophys. Res.*, **92**, 4971–5029.
- , J. Hamilton, and W. H. Hui, 1985: Directional spectra of wind-generated waves. *Philos. Trans. Roy. Soc. London*, **315A**, 509–562.
- Donnelly, W. J., J. R. Carswell, R. E. McIntosh, P. S. Chang, J. Wilkerson, F. Marks, and P. G. Black, 1999: Revised ocean backscatter models at C and Ku band under high-wind conditions. *J. Geophys. Res.*, **104** (C5), 11 485–11 497.
- Dulov, V. A., and M. V. Kosnik, 2009: Effects of three-wave interactions in the gravity-capillary range of wind waves. *Izv. Atmos. Oceanic Phys.*, **45**, 380–391.
- Durden, S. L., and J. F. Vesecky, 1985: A physical radar cross-section model for a wind-driven sea with swell. *IEEE J. Oceanic Eng.*, **10**, 445–451.
- Ebuchi, N., and S. Kizu, 2002: Probability distribution of surface wave slope derived using sun glitter images from geostationary meteorological satellite and surface vector winds from scatterometers. *J. Oceanogr.*, **58**, 477–486.
- , H. Kawamura, and Y. Toba, 1987: Fine structure of laboratory wind-wave surfaces studied using an optical method. *Bound.-Layer Meteor.*, **39**, 133–151.
- Elfouhaily, T., B. Chapron, K. Katsaros, and D. Vandemark, 1997: A unified directional spectrum for long and short wind-driven waves. *J. Geophys. Res.*, **102** (C7), 15 781–15 796.
- Felizardo, F., and W. K. Melville, 1995: Correlations between ambient noise and the ocean surface wave field. *J. Phys. Oceanogr.*, **25**, 513–532.
- Fung, A. K., and K. K. Lee, 1982: A semi-empirical sea-spectrum model for scattering coefficient estimation. *IEEE J. Oceanic Eng.*, **7**, 166–176.
- García-Nava, H., F. J. Ocampo-Torres, P. Osuna, and M. A. Donelan, 2009: Wind stress in the presence of swell under moderate to strong wind conditions. *J. Geophys. Res.*, **114**, C12008, doi:10.1029/2009JC005389.
- Geernaert, G. L., 1990: Bulk parameterizations for the wind stress and heat fluxes. *Current Theory*, G. L. Geernaert and W. J. Plant, Eds., *Surface Waves and Fluxes*, Vol. 1, Kluwer Academic, 91–172.
- Hara, T., E. J. Bock, J. B. Edson, and W. R. McGillis, 1998: Observation of short wind waves in coastal waters. *J. Phys. Oceanogr.*, **28**, 1425–1438.
- Hasselmann, K., and Coauthors, 1973: Measurements of wind-wave growth and swell decay during the Joint North Sea Wave Project (JONSWAP). *Dtsch. Hydrogr. Z.*, **A8** (Suppl.), 1–95.
- Hauser, D., G. Caudal, S. Guimard, and A. A. Mouche, 2008: A study of the slope probability density function of the ocean waves from radar observations. *J. Geophys. Res.*, **113**, C02006, doi:10.1029/2007JC004264.
- Hersbach, H., A. Stoffelen, and S. de Haan, 2007: An improved C-band scatterometer ocean geophysical model function: CMOD5. *J. Geophys. Res.*, **112**, C03006, doi:10.1029/2006JC003743.
- Holthuijsen, L. H., M. D. Powell, and J. D. Pietrzak, 2012: Wind and waves in extreme hurricanes. *J. Geophys. Res.*, **117**, C09003, doi:10.1029/2012JC007983.
- Hughes, B. A., and H. L. Grant, 1978: The effect of internal waves on surface wind waves 1. Experimental measurements. *J. Geophys. Res.*, **83** (C1), 443–454.
- Hwang, P. A., 1997: A study of the wavenumber spectra of short water waves in the ocean. Part II: Spectral model and mean square slope. *J. Atmos. Oceanic Technol.*, **14**, 1174–1186.
- , 2005: Wave number spectrum and mean square slope of intermediate-scale ocean surface waves. *J. Geophys. Res.*, **110**, C10029, doi:10.1029/2005JC003002.
- , 2006: Doppler frequency shift in ocean wave measurements: Frequency downshift of a wavenumber component by advection of background wave orbital velocity. *J. Geophys. Res.*, **111**, C06033, doi:10.1029/2005JC003072.
- , 2007: Spectral signature of wave breaking in surface wave components of intermediate length scale. *J. Mar. Syst.*, **66**, 28–37.
- , 2008: Observations of swell influence on ocean surface roughness. *J. Geophys. Res.*, **113**, C12024, doi:10.1029/2008JC005075.
- , 2011: A note on the ocean surface roughness spectrum. *J. Atmos. Oceanic Technol.*, **28**, 436–443.
- , 2012: Foam and roughness effects on passive microwave remote sensing of the ocean. *IEEE Trans. Geosci. Remote Sens.*, **50**, 2978–2985, doi:10.1109/TGRS.2011.2177666.
- , and D. W. Wang, 2001: Directional distributions and mean square slopes in the equilibrium and saturation ranges of the wave spectrum. *J. Phys. Oceanogr.*, **31**, 1346–1360.
- , and —, 2004a: An empirical investigation of source term balance of small scale surface waves. *Geophys. Res. Lett.*, **31**, L15301, doi:10.1029/2004GL020080.
- , and —, 2004b: Field measurements of duration limited growth of wind-generated ocean surface waves at young stage of development. *J. Phys. Oceanogr.*, **34**, 2316–2326; Corrigendum, **35**, 268–270.
- , and W. J. Plant, 2010: An analysis of the effects of swell and roughness spectra on microwave backscatter from the ocean. *J. Geophys. Res.*, **115**, C04014, doi:10.1029/2009JC005558.
- , D. B. Trizna, and J. Wu, 1993: Spatial measurements of short wind waves using a scanning slope sensor. *Dyn. Atmos. Oceans*, **20**, 1–23.
- , S. Atakturk, M. A. Sletten, and D. B. Trizna, 1996: A study of the wavenumber spectra of short water waves in the ocean. *J. Phys. Oceanogr.*, **26**, 1266–1285.
- , W. J. Teague, G. A. Jacobs, and D. W. Wang, 1998: A statistical comparison of wind speed, wave height and wave period derived from satellite altimeters and ocean buoys in the Gulf of Mexico region. *J. Geophys. Res.*, **103** (C5), 10 451–10 468.
- , M. A. Sletten, and J. V. Toporkov, 2008: Breaking wave contribution to low grazing angle radar backscatter from the

- ocean surface. *J. Geophys. Res.*, **113**, C09017, doi:10.1029/2008JC004752.
- , B. Zhang, J. V. Toporkov, and W. Perrie, 2010: Comparison of composite Bragg theory and quad-polarization radar backscatter from RADARSAT-2: With applications to wave breaking and high wind retrieval. *J. Geophys. Res.*, **115**, C08019, doi:10.1029/2009JC005995; Corrigendum, **115**, C11099, doi:10.1029/2010JC006653
- , D. M. Burrage, D. W. Wang, and J. C. Wesson, 2011a: An advanced roughness spectrum for computing microwave L-band emissivity in sea surface salinity retrieval. *IEEE Geosci. Remote Sens. Lett.*, **8**, 547–551, doi:10.1109/LGRS.2010.2091393.
- , H. García-Nava, and F. J. Ocampo-Torres, 2011b: Dimensionally consistent similarity relation of ocean surface friction coefficient in mixed seas. *J. Phys. Oceanogr.*, **41**, 1227–1238.
- Isoguchi, O., and M. Shimada, 2009: An L-band ocean geophysical model function derived from PALSAR. *IEEE Trans. Geosci. Remote Sens.*, **47**, 1925–1936.
- Jackson, F. C., W. T. Walton, D. E. Hines, B. A. Walter, and C. Y. Peng, 1992: Sea surface mean-square slope from K_u -band backscatter data. *J. Geophys. Res.*, **97** (C7), 11 411–11 427.
- Jähne, B., and K. S. Riemer, 1990: Two-dimensional wave number spectra of small-scale water surface waves. *J. Geophys. Res.*, **95** (C7), 11 531–11 546.
- Janssen, J. A. M., 1997: Does wind stress depend on sea-state or not?—A statistical error analysis of HEXMAX data. *Bound.-Layer Meteor.*, **83**, 479–503.
- Janssen, P. A. E. M., 1987: The initial evolution of gravity-capillary waves. *J. Fluid Mech.*, **184**, 581–597, doi:10.1017/S0022112087003033.
- Jarosoz, E., D. A. Mitchell, D. W. Wang, and W. J. Teague, 2007: Bottom-up determination of air-sea momentum exchange under a major tropical cyclone. *Science*, **315**, 1707–1709.
- Jonathan, P., J. Flynn, and K. Evans, 2010: Joint modelling of wave spectral parameters for extreme sea states. *Ocean Eng.*, **37**, 1070–1080.
- Jones, W. L., and L. C. Schroeder, 1978: Radar backscatter from the ocean: Dependence on surface friction velocity. *Bound.-Layer Meteor.*, **13**, 133–149.
- Keller, W. C., and J. W. Wright, 1975: Microwave scattering and the straining of wind-generated waves. *Radio Sci.*, **10**, 139–147.
- Klinke, J., and B. Jähne, 1995: Measurements of short wind waves during the MBLARI west coast experiment. *Air-Water Gas Transfer*, B. Jähne and E. C. Monahan, Eds., AEON Verlag and Studio, 165–173.
- Kudryavtsev, V., V. Makin, and B. Chapron, 1999: Coupled sea surface atmosphere model: 2. Spectrum of short wind waves. *J. Geophys. Res.*, **104** (C4), 7625–7639.
- Large, W. G., and S. Pond, 1982: Sensible and latent heat flux measurements over the ocean. *J. Phys. Oceanogr.*, **12**, 464–482.
- Longuet-Higgins, M. S., 1963: The generation of capillary waves by steep gravity waves. *J. Fluid Mech.*, **16**, 138–159.
- , 1992: Capillary rollers and bores. *J. Fluid Mech.*, **240**, 659–679.
- , and J. S. Turner, 1974: An ‘entraining plume’ model of a spilling breaker. *J. Fluid Mech.*, **63**, 1–20.
- McGoldrick, L. F., 1965: Resonant interactions among capillary-gravity waves. *J. Fluid Mech.*, **21**, 305–332.
- , 1970: An experiment on second-order capillary gravity resonant wave interactions. *J. Fluid Mech.*, **40**, 251–271.
- Meissner, T., and F. J. Wentz, 2009: Wind-vector retrievals under rain with passive satellite microwave radiometers. *IEEE Trans. Geosci. Remote Sens.*, **47**, 3065–3083.
- Merzi, N., and W. H. Graf, 1985: Evaluation of the drag coefficient considering the effects of mobility of the roughness elements. *Ann. Geophys.*, **3**, 473–478.
- Miles, J. W., 1957: On the generation of surface waves by shear flow. *J. Fluid Mech.*, **3**, 185–204.
- Munk, W., 2009: An inconvenient sea truth: Spread, steepness, and skewness of surface slopes. *Annu. Rev. Mar. Sci.*, **1**, 377–415.
- Okuda, K., S. Kawai, and Y. Toba, 1977: Measurement of skin friction distribution along the surface of wind waves. *J. Oceanogr. Soc. Japan*, **33**, 190–198.
- Phillips, O. M., 1958: The equilibrium range in the spectrum of wind-generated waves. *J. Fluid Mech.*, **4**, 426–434.
- , 1984: On the response of short ocean wave components at a fixed wavenumber to ocean current variations. *J. Phys. Oceanogr.*, **14**, 1425–1433.
- , 1985: Spectral and statistical properties of the equilibrium range in wind-generated gravity waves. *J. Fluid Mech.*, **156**, 505–531.
- Pierson, W. J., and L. Moskowitz, 1964: A proposed spectral form for full, developed wind seas based on the similarity theory of S. A. Kitaigorodskii. *J. Geophys. Res.*, **69** (24), 5181–5190.
- , and R. A. Stacy, 1973: The elevation, slope and curvature spectra of a wind roughened sea surface. NASA Contract Rep. CR-2247, 126 pp.
- Plant, W. J., 1977: Studies of backscattered sea return with a CW dual-frequency, X-band radar. *IEEE J. Oceanic Eng.*, **2**, 28–36.
- , 1982: A relationship between wind stress and wave slope. *J. Geophys. Res.*, **87** (C3), 1961–1967.
- , 1990: Bragg scattering of electromagnetic waves from the air/sea interface. *Remote Sensing*, G. L. Geernaert and W. J. Plant, Eds., Vol. 2, *Surface Waves and Fluxes*, Kluwer Academic Publishers, 41–108.
- , 2002: A stochastic, multiscale model of microwave backscatter from the ocean. *J. Geophys. Res.*, **107**, C93120, doi:10.1029/2001JC000909.
- , and J. W. Wright, 1977: Growth and equilibrium of short gravity waves in a wind-wave tank. *J. Fluid Mech.*, **82**, 767–793.
- , and —, 1979: Spectral decomposition of short gravity wave systems. *J. Phys. Oceanogr.*, **9**, 621–624.
- , and —, 1980: Phase speeds of upwind and downwind traveling short gravity waves. *J. Geophys. Res.*, **85** (C6), 3304–3310.
- Powell, M. D., P. J. Vickery, and T. A. Reinhold, 2003: Reduced drag coefficient for high wind speeds in tropical cyclones. *Nature*, **422**, 279–283.
- Ricciardulli, L., and F. Wentz, 2011: Reprocessed QuikSCAT (V04) wind vectors with Ku-2011 geophysical model function. Remote Sensing Systems Tech. Rep. 043011, 8 pp.
- , T. Meissner, and F. Wentz, 2012: Towards a climate data record of satellite ocean vector winds. *Proc. 2012 IEEE Int. Geoscience and Remote Sensing Symp.*, Munich, Germany, IEEE, 2067–2069.
- Romeiser, R., W. Alpers, and V. Wismann, 1997: An improved composite surface model for the radar backscattering cross section of the ocean surface. 1. Theory of the model and optimization/validate by scatterometer data. *J. Geophys. Res.*, **102** (C11), 25 237–25 250.
- Ross, V., and D. Dion, 2007: Sea surface slope statistics derived from sun glitter radiance measurements and their apparent dependence on sensor elevation. *J. Geophys. Res.*, **112**, C09015, doi:10.1029/2007JC004137.

- Shemdin, O. H., and P. A. Hwang, 1988: Comparison of measured and predicted sea surface spectrum of short waves. *J. Geophys. Res.*, **93** (C11), 13 883–13 890.
- , H. M. Tran, and S. C. Wu, 1988: Directional measurement of short ocean waves with stereophotography. *J. Geophys. Res.*, **93**, 13 891–13 901.
- Simmons, W. F., 1967: A variational method for weak resonant wave interactions. *Proc. Roy. Soc. London*, **309A**, 551–579.
- Stiassnie, M., 1996: On the equilibrium spectrum of gravity-capillary waves. *J. Phys. Oceanogr.*, **26**, 1093–1098.
- Tang, S., and O. H. Shemdin, 1983: Measurement of high frequency waves using a wave follower. *J. Geophys. Res.*, **88** (C14), 9832–9840.
- Terray, E. A., M. A. Donelan, Y. C. Agrawal, W. M. Drennan, K. K. Kahma, A. J. Williams, P. A. Hwang, and S. A. Kitaigorodskii, 1996: Estimates of kinetic energy dissipation under breaking waves. *J. Phys. Oceanogr.*, **26**, 792–807.
- Trokhimovski, Y. G., and V. G. Irisov, 2000: The analysis of wind exponents retrieved from microwave radar and radiometric measurements. *IEEE Trans. Geosci. Remote Sens.*, **38**, 470–479.
- Valenzuela, G. R., 1978: Theories for the interaction of electromagnetic and oceanic waves—A review. *Bound.-Layer Meteor.*, **13**, 61–85.
- , and L. B. Laing, 1972: Nonlinear energy transfer in gravity-capillary wave spectra with applications. *J. Fluid Mech.*, **54**, 507–520.
- Vandemark, D., B. Chapron, J. Sun, G. H. Crescenti, and H. C. Graber, 2004: Ocean wave slope observations using radar backscatter and laser altimeters. *J. Phys. Oceanogr.*, **34**, 2825–2842.
- van Gastel, K., 1987: Nonlinear interactions of gravity-capillary waves: Lagrangian theory and effects on the spectrum. *J. Fluid Mech.*, **182**, 499–523, doi:10.1017/S002211208700243X.
- Vickery, P. J., D. Wadhera, M. D. Powell, and Y. Chen, 2009: A hurricane boundary layer and wind field model for use in engineering application. *J. Appl. Meteor. Climatol.*, **48**, 381–405.
- Walsh, E. J., D. C. Vandemark, C. A. Friehe, S. P. Burns, D. Khelif, R. N. Swift, and J. F. Scott, 1998: Measuring sea surface mean square slope with a 36-GHz scanning radar altimeter. *J. Geophys. Res.*, **103** (C6), 12 587–12 601.
- WAMDI group, 1988: The WAM model—A third generation ocean wave prediction model. *J. Phys. Oceanogr.*, **18**, 1775–1810.
- Wang, D. W., and P. A. Hwang, 2004: On the dispersion relation of short gravity waves from space–time wave measurements. *J. Atmos. Oceanic Technol.*, **21**, 1936–1946.
- Wentz, F. J., 1977: A two scale scattering model with application to the JONSWAP '75 aircraft microwave scatterometer experiment. NASA Contract Rep. 2919, 122 pp.
- , and D. K. Smith, 1999: A model function for the ocean-normalized radar cross section at 14 GHz derived from NSCAT observations. *J. Geophys. Res.*, **104** (C5), 11 499–11 514.
- Wright, C. W., and Coauthors, 2001: Hurricane directional wave spectrum spatial variation in the open ocean. *J. Phys. Oceanogr.*, **31**, 2472–2488.
- Wright, J. W., 1966: Backscattering from capillary waves with application to sea clutter. *IEEE Trans. Antennas Propag.*, **14**, 749–754.
- , 1968: A new model for sea clutter. *IEEE Trans. Antennas Propag.*, **16**, 217–223.
- , 1978: Detection of ocean waves by microwave radars: The modulation of short gravity-capillary waves. *Bound.-Layer Meteor.*, **13**, 87–105.
- Wu, J., 1980: Wind-stress coefficients over sea surface near neutral conditions—A revisit. *J. Phys. Oceanogr.*, **10**, 727–740.
- Yueh, S. H., S. J. Dinardo, A. G. Fore, and F. K. Li, 2010: Passive and active L-band microwave observations and modeling of ocean surface winds. *IEEE Trans. Geosci. Remote Sens.*, **48**, 3087–3100.
- Zappa, C. J., M. L. Banner, H. Schultz, A. Corrada-Emmanuel, L. B. Wolff, and J. Yalcin, 2008: Retrieval of short ocean wave slope using polarimetric imaging. *Meas. Sci. Technol.*, **19**, 055503, doi:10.1088/0957-0233/19/055503.
- , —, —, J. R. Gemmrich, R. P. Morrison, D. A. LaBel, and T. Dickey, 2012: An overview of sea state conditions and air-sea fluxes during RaDyO. *J. Geophys. Res.*, **117**, C00H19, doi:10.1029/2011JC007336.
- Zhang, X., 1995: Capillary-gravity and capillary waves generated in a wind wave tank: Observations and theories. *J. Fluid Mech.*, **289**, 51–82.
- , 2003: Surface image velocimetry for measuring short wind wave kinematics. *Exp. Fluids*, **35**, 653–665.
- , 2005: Short surface waves on surface shear. *J. Fluid Mech.*, **541**, 345–370.